.

.

Thesis To Applied for the Grade of Master of Science in Applied Physics

Albert-Ludwigs-Universität Freiburg

Faculty of Physics

Single Shot correlation in VMI- TOF measurements on He nanodroplets at MIR femtosecond laser pulses

Presented by   Cristian Enrique Medina Hernandez

Date   15. febrary 2019

Referent   Prof. Dr. Marcel Mudrich and Prof. Dr. Frank Stinkermeier

Abstract

In this thesis a new data acquisition method is explained for correlate single shot VMI-TOF measurements on He droplets ionized by a MIR femtosecond laser. Until now VMI images and TOF data are always treated in a statistical way. Whit these new method we expect to have some better correlation for single explosion and relate each of the event from a individual way, having specific information that could be lost in the statistical method. The correlated data is acquired by triggering the VMI camera and the TOF oscilloscope with the laser trigger, so both acquisitions begging and end after the same laser pulse. Results for the energies.............here a resumy of the results.........

Contents

List of abbreviations

ATI   above threshold ionization

BSI   barrier suppression ionization

CCD   Charge-coupled Device

CPA   Chirp Pulse Amplification

CWL   Central wavelength

EM   Electro Mechanics

LASER   Light Amplification by Stimulated Emission of Radiation

LT   Langmuir-Taylor

MCP   Micro Channel Plate

NIR   Near Infrared

pBASEX polar Basis Set Expansion

PID   Proportional – Integral – Derivative

TBR   Three Body Recombination

TOF   Time of flight

VMI   Velocity Map Imaging

VUV   vacuum ultra violet

XUV   Extreme ultraviolet

0.1 Introduction

Physicists have always wonder to explain and resolve dynamic processes in short times, to characterize in a time evolution scale fast processes indistinguishable to us. Describe these systems requires to acquire data in brief time windows, for example, a film is only a consecutive sequence of photographs that recreate a large time laps in a smaller time scale. For atomic physics, we are talking about a micro-cosmos that varies from microseconds to attoseconds, i.e in atoms where time scales can go down to $10^{-9}s$.

The dynamics time window of a system is related to its quantum dynamics, in other words, to its size. For dynamics happening in a molecule or a many body system interaction, times can oscillate between microseconds to nanoseconds. from an energetic point of view, systems on the milielectronvolt scale (meV) for its energy levels, implies that molecular vibrations occurs on a time scale of tens to hundreds of femtoseconds. In smaller complex, motion of individual electrons in semiconductor nano structures, molecular orbitals, and the inner shells of atoms occurs on progressively shorter intervals of time, ranging from tens of femtoseconds to less than an attosecond. Motion within nuclei is predicted to unfold even faster, typically on a zeptosecond time scale.

To achive this higth resolution in space-time physicist have challenged to create systems with a well controlled spatial and temporal gradient. Fortunately nowadays, laser pulses can research up to extreme non-linear optical processes, producing single aisolated pulses of ultra violet(UV) waves as short as $67as$ [67]. Such fast pulses open up the possibility of time resolved measurements fort short processes like electron dynamics. However, to do this, experimental schemes must be devised that allow these new light sources to be used to perform measurements on the microcosmos. In particular, in the last few years, many studies at atom- and molecule-clusters had been published, from mid-infre red (NIR) interaction to UV or XUV pulses, that not just lead to a broad spectra to study, but also to a large range of possible applications such as the generation of energetic electrons and ions in the keV-regime [18], as well as intensive XUV and attosecond pulses [55]. Laser pulses with peak intensities up to 10^{21} W/cm^2 are available nowadays [45] commercially so the difficulty and expensive of the experiments source also are easy.

Femtosecond lasers are a milestone in order to control and ignite atomic processes in controlled standard,but acquire the information is also a huge challenge. Now a days, several techniques are available depending the nature of the process. For this particular work we are interested in two techniques, Velocity map image (VMI) and Time of flight (TOF). Since its invention, this techniques has become two of the

most commune and important measurement techniques in high energies physics....
But detecting a signal is just one part of the job, the new laser advances like the
generation of coherent high-intensity laser pulses with intensities up to $10^{22}W/cm^2$
allow multiphoton ionization that allows to get time resolved measurements. These
advances have enabled the development of new research areas, as well as the inves-
tigation of ultrafast dynamics in highly excited matter to nanometer size.

In this thesis, we focus our efforts on the ionization processes by Mid Infrared
(MIR) femtosecond pulses in doped noble gases clusters. The interaction of the
dopant with the laser field result in a energy transfer to the droplet that ignite a
ionization process, known as a nanoplasma. This resonant interaction of the laser
field with a collective oscillation of the electrons in the plasma is driven by the laser
field [18]. This process, caused predominantly by electron impact ionization, makes
an avalanche-like ionization of the atoms in the cluster, leading to a heating of the
plasma and, as a result, to hydrodynamic expansion and Coulomb explosion. To
the analysis of this process we studied the electrons as well as the ion's resulting
in the coulomb explosion. A velocity map imaging and a Time of flight technique
are set up in parallel to acquire the data and reconstruct the initial energies and
configuration of the plasma in study. In the First chapter we will present a brief
introduction to the Droplet He generation, a short plasma interactions as a basic
background of coulomb ionization in order to understand the physical meaning. In
the second chapter a more detailed explanation of the set-up used. Showing from
the creation of the He droplets process to its detection , going thorough the doping,
and ignition process. Finally, a detailed explanation on the correlation method for
the VMI-TOF measurements is done, showing the set-up of the data acquisition and
its advantages.

In the third chapter we show the correlated data and its analysis, introducing
the calibration methods, data processing and results. Finally, in the last chapter
we present the summary and outcome of the experiments as well as the inputs for
future works to improve the results.

1 Theoretical Background

In the following chapter we will present all the theoretical background necessary for the development of this project, from the theory and creation of the He and Ne droplets to the physics theories of plasma and cluster coulomb explosion processes including its detection techniques. In order to guide the reader in an organised way, the chapters are organized in a way that follow the processes necessaries to the performance of the experiment.

1.1 Helium Nanodroplets

The combination of cryogenic matrix isolation, discovered in 1954 [64], and the now well defined properties of Helium (He), specially its superfluidity face discovered in 1937 by *Kapitza et. all* [32], have as consequence one of the most powerful and flexible tool in physics, the helium nanodroplets. Helium nanodrops have unique properties that makes it a unique source for the cluster and nanophysics experiments in the last decades. For example, they do not exhibit any optical transitions in the entire infrared, visible and ultraviolet range. They can readily pick up atoms and molecules and form different complexes of the species embedded in their interior or on their surfaces, acting as a ideal matrix for atoms, molecules and clusters isolation. [56] [61]. The size of a He cluster can go from of a few thousands up to 10^8 of atoms, and reach the ultra cold temperature regime (close to $0.37K$ [60]) [15]. Two main advantages of this cooling properties arise. First, dopants in the He nanodroplet are set to their absolute vibronic ground states, avoiding all other possible espectra and stablishing the cluster in a specific state, more important, the fast cooling helps to the formation of isomers that are difficult or impossible to generate with other methods [46]. Second, because the superfluid fase of the He nanodroplets [22], the bond between dopants and He is weak. Therefore, in contrast to spectroscopy in other matrices with higher temperatures, the optical transitions of many dopants are barely influenced by the He matrix [61]. The theory of He superfluidity will not be part of this section, this imformation is well documented in other sources, and here we are based on ref. [15] where all theory is well presented to the reader. In the

next section we will dedicate a bigger effort to explain the theoretical and technical background of the He nanodroplets creation as well as the physical and technical process to doped it.

1.1.1 He Nano droplets production

At room temperature, helium is a light inert gas. It is odorless, colorless, tasteless, and after hydrogen, the second most abundant element in the universe. [15]. It have a simple 2 atoms structure, exhibing numerous exotic phenomena whose theoretical descriptions are rather complex in many cases, i.e it characteristics of a quantum fluid. From helium exist two stable isotopes ^3He and ^4He. ^4He has two electrons, two protons and two neutrons, no nuclear spin and no total spin, pertaining to the bosonic family, while ^3He with only one neutron has a spin of $I = 1/2$ and belongs to the fermions [4].

The bosonic state $_4He$ is specially of interest, at temperature T$\leqslant$2.8K and under normal pressure has a phase transition from "normal liquid" He-I to super liquid He-II [58], in which the helium can be described by a Bose-Einstein condensation. Even the fermionic ^3He exhibits this phase transition at T$\leqslant 0.03K$ [27].

The superfluidity of $He - II$, at temperatures close to absolute zero, brings with it some unique features. The essential Properties for this include an almost disappearing viscosity in the superfluid phase, weak interaction, very efficient cooling, and the Transparency for electromagnetic radiation up to wavelengths in vacuum ultraviolets (VUV) Spectral range [15]. Helium has therefore in the complete visible spectrum no transitions from the ground state. Through the noble gas configuration, helium has a spherically symmetrical electron distribution [40], it can hardly be polarized and is the least reactive of all the elements.

1.1.1.1 Helium Droplets

The production He droplets had to overcome first one principal problem, its liquefaction. At the end of 19th century many gases were liquefied for the first time by applying pressure at room temperature. However, for He and hydrogen, this method was not successful. In 1922 Kamerlingh Onnes reached temperatures below $1K$ by reducing the vapor pressure above liquid helium to about $2*10^{-5}$ bar with a series of pumps [11]. The Joule–Thomson effect [63] is in this case the responsible for Onnes experiment to reach this low temperatures. The basic idea is that under suitable conditions a gas in expanding performs work against its internal forces. Basically the gas is expanded through a small nozzle thermally isolated from its surroundings.

Figure 1.1: ^4He Phase transition at Ultra cold temperatures. ^4He is the more common isotope of helium. It remains liquid at zero temperature if the pressure is below $2.5MPa$. The liquid has a phase transition to a super-fluid phase, also known as He-II, at the temperature of $2.17K$ (at vapor pressure). Taken from [1]
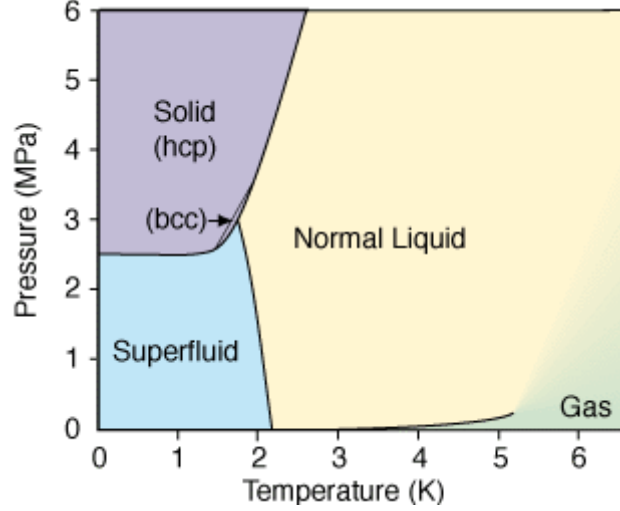
The expansion under theses conditions takes place at constant enthalpy, since the expansion nozzle performs no work. following the next relation:

$$W = H_1 - H_2 = (U_1 + p_1V_1) - (U_2 + p_2V_2) \tag{1.1}$$

where H is the entalpy before and after, $U = \dfrac{3}{2}Nk_bT$ for ideal gases and $pV = Nk_bT$ [15]. Under Joule–Thomson effect conditions, $W = 0$ so $H_1 = H_2$, this expansion leads to a cooling or a warming and under certain conditions, becomes supersaturated. As a result, condensation takes place and a beam of clusters is formed.

Helium nanodroplets are typically produced by a continuous or pulsed adiabatic Expansion of pre−cooled helium through a small aperture from a reservoir into a vacuum [56]. In this process a droplet jet is formed, and its characteristics (blasting speeds and size distribution) can be changes due the manipulation of the set−up. For example, $\triangle$ pressure between the reservoir and the vacuum chamber (usually in the range of a few to $10MPa$) , the nozzle temperatures(from a few K to $T \leqslant 40K$) or the nozzle size (with pinholes of diameter rounding $5 - 20\mu m$).

When the Helium expands from the nozzel, its thermal energy is transform in kinetic energy of a supersonic flow field. After the expantion into the vacuum, the gas becomes supersaturated and condensations starts to occurs, creating the beam clusters. This clusters are made of atoms or moleulces held togueter by Wannder
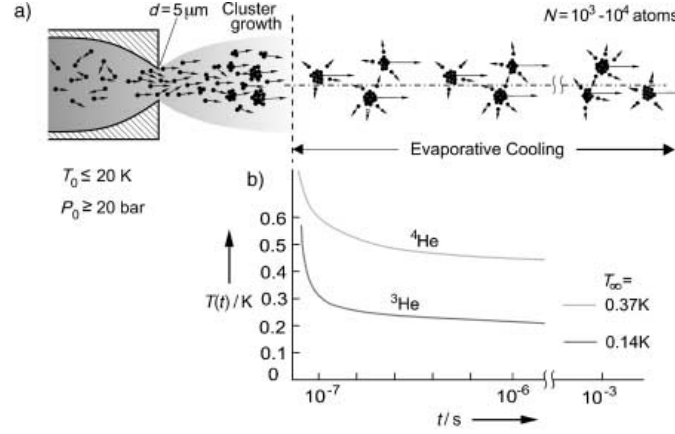
Figure 1.2: a) Schematic representation of the processes leading to the formation and subsequent cooling of helium droplets in a gas expansion. b) Calculated dependence of the droplet temperature on time for ^4He and ^3He droplets after they have left the cluster, taken from [61]
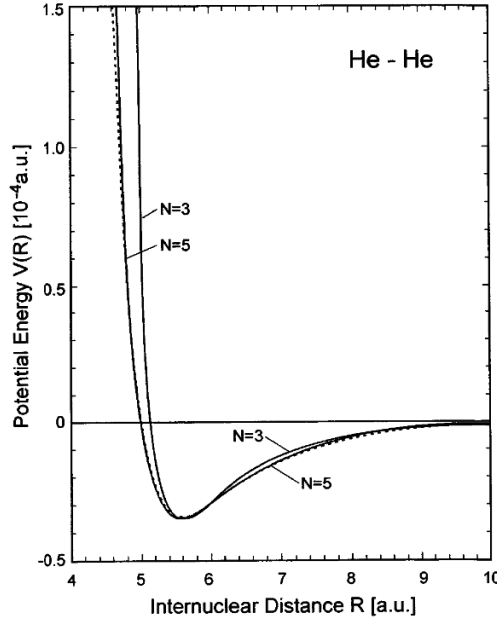

Figure 1.3: Waan der Wals potential for He-He interaction

wals fores, in this case He-He interaction, that share the same kinetic vector. This means that the two particules travel as close and parallel to each other that a bonding is possible, see fig 1.3. From the reference frame of the cluster, each of its molecules are close to cero movments, in He this enhace the conditions to be liquid and in consecience superfluidity is achive [25].

Depending on the buffer gas used, the mechanisms for cluster formation in the supersonic expansion range from condensation from the gas phase to fragmentation of a liquid phase. figure ?? show how to distinguish between these two limiting

11

conditions. In the case the expansion is isentropic (adiabatic and reversible), the expansion is represented by a vertical line in this diagram. Clusters formed by condensation from the gas phase occur when the expansion crosses into the two-phase region on the right-hand side of the critical point. Clusters formed by fragmentation of the liquid phase occur when the expansion crosses into the two-phase region on the left hand side of the critical point. the diagram is an example of three gases, He, Ar and H2 at diferent pressures ($p' = P/P_{critical}$,) [35]. the curves represents the regions where the supersonic expansion cam be done and the temperatures (in Fig dimensionles)that each gas should have in order to achive clustering and cooling. [35]
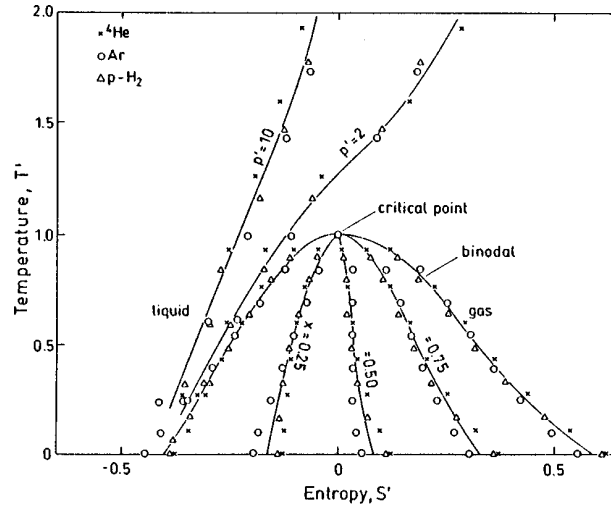

Figure 1.4: Dimensionless phase diagram for He, H2 and Ar. where T is dimensionless $T' = (T - T_{tp})/(T_{cr} - T_{tp})$, same as entropy $S' = (S - S_{cr})/\Delta Stp$ and $x = fraction$ of the fluid in the gaseous phase, where the subscripts cr and tp refer to the critical point and the triple point, and ΔS is the entropy change for vaporization. The curves are drawn as guides to the eye not exact measuments, taken from [35].

There is no mathematical approach of the physics behind this cooling expansion but usually, Raleigh scattering measurements in combination with an empirical scaling law [25] are used to estimate the mean cluster size giving a certain degree of control over the cluster size distribution by adjusting the nozzle width and the source pressure. The droplet size distribution during supersonic expansion in the follows a log-normal distribution of the form [28].

$$p(N) = \frac{1}{\sqrt{2\pi}N\sigma} \exp\left[-\frac{(ln(N/N_0)^2}{2\sigma^2}\right] \qquad (1.2)$$

Where N is the number of atom in the cluster, σ is the distribution width and N_0

is the most likely numbers of atoms. Following it give a mean value.

$$\bar{N} = \exp\left(\mu + \frac{\sigma^2}{2}\right) \tag{1.3}$$

With a half width maxima of [28]

$$\sigma N_{\frac{1}{2}} = \exp\left(\mu - \sigma^2 + \sigma\sqrt{2ln(2)}\right) - \exp\left(\mu - \sigma^2 - \sigma\sqrt{2ln(2)}\right) \tag{1.4}$$

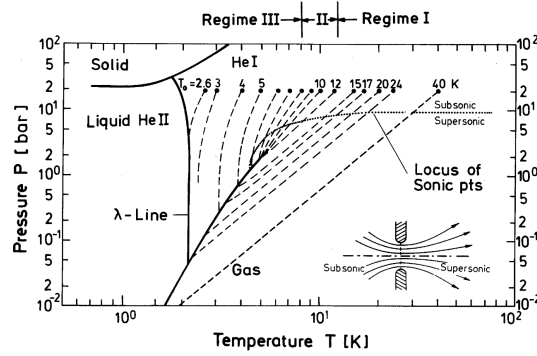

Figure 1.5: Expansion regimes. Pressure-Temperatur phase diagram for ^4He for Nozzle beam expansions starting from a stagnation of 20 bar and a temperatures. As dicusse, quialitatively different behaivors are shown for the regime I - II and II where starting in the gas phase, near the phase trnasition respectivelly. taken from [7].

As show in Figure ?? The conditions in the He (pressure, temperature and nozzle size) in the free expansion will determine the characteristics of our final He beam. From Here three main regimes can be define.

Regime I or sub-critical expansion, begins in the gas phase and leads to droplet formation via condensation. this is the case of most expansions since the pressure are located below the critical pressure P_c. Regime II, also called as critical expansion, is basically and interminable regime that includes all trajectories which are near the critical point, leading to random expansion and difficult control of the beam due the large fluctuations in density. Regime III, the supercritical expansion, starts at low temperatures where the He stops behaving as an ideal gas, expecting flashing or cavitation breaking up the liquid drops jet. [7]

super-critical and sub-critical regimes have been studies in the last several years and are clearly identified in the resulting size distributions. Figure ?? shows that supercritical expansion forms large droplets (usually between $20 - 100nm$ diameter) while a sub-critical expansion is suited to generate small droplets (around $5-10nm$). A simple relation that can be done to calculate the size or number of atom in a Custer

is using.

$$r = N_{1/3} * \rho A \tag{1.5}$$

Where r is the radius of the beam, ρ is the density, in thhis case of He $\rho = 0.0022A$ [57], but this approximation is not exact due the variation Of He density at this temperatures. As expected in both regimens for creating larger helium nano droplets, higher helium pressure and lower nozzle temperature are used. For our experiment a $5\mu m$ nozzle was used at temperature oscillating between $11 - 15K$, at pressure of $30 to 50$ bar.

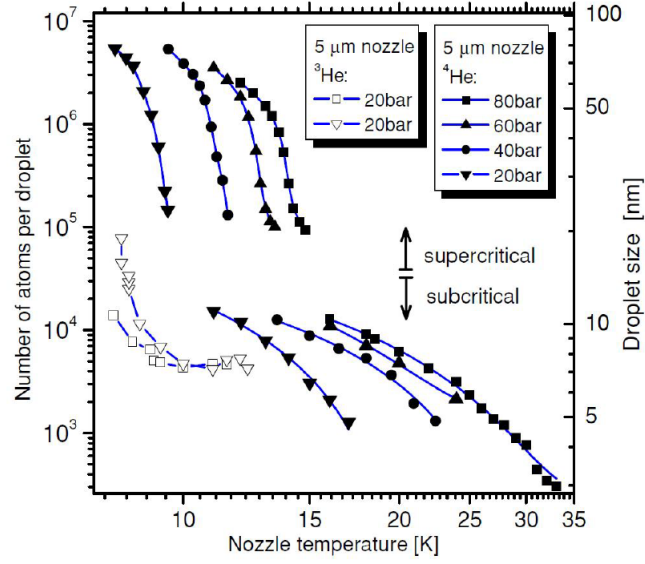Figure 1.6: Sizes of the ^4He droplets as a function of nozzle temperature T and pressures, based on [60], using a $5\mu m$ nozzle. The sub and super critical regimes are clearly diferenciated. Taken from [?]

1.1.1.2 Composite Clusters

We can define a composite cluster or doped cluster, as a atom bulk of one material that contains one or more different atomic elements. The main interesting properties in non doped clusters are usually set as a function of its size, but for doped clusters, the interaction between the elements creates new degrees of freedom that makes more complex its behaviour. For example, the new composite will have different structural properties due the spatial distribution of the species. Hence, composite clusters exhibit a more diverse behaviour and offer more opportunities to study different characteristics of the material.

The first problem to overcome in composite cluster is how to create them. Two techniques can be used. The first one, is the co expansion of a previously mixed gas [59] or the He cluster is produced first and then crossed with an atomic beam of the doping species.

The first technique involves several technical problems, depends on possible interactions between the elements, the condensation ranges of the bulks and even in the affinity of the materials. One of the most used techniques, and the one used in this study is the one called pick-up technique [21]. The idea is simple, as well as a snowball on its way downhill collects or pick-up more snow. The He cluster, after being directional selected through a Skimmer, passes through a doping cell with a dopant gas at low densities $(10 - 2Pa)$ [56]. As a result, the gas atoms that are along the droplet cross sections will be captured by the beam and travel with it. The probability for helium droplets to collect k atoms or molecules via inelastic collisions depends on the length of the oven cell l, the cross section of the droplets σ, and the particle density inside the cell n. As l and σ remains constant, varying the density in the doping cell can regulated the abundance of k, following the Poissonian statistics.

$$P_k(l, n, \sigma) = \frac{(ln\sigma)^k}{k!} e^{(-ln\sigma)} \tag{1.6}$$

Two important properties of these relation can be infer. First the maxima of different cluster sizes are equidistant, $n_{max} = \dfrac{k}{l\sigma}$ and second, the exponential function in equation becomes nearly one for small particle densities [6].

Every pick-up process leads to an energy transfer to the droplets. As the dopant rapidly cool down to their, it means a transfer of energy to the He causing an evaporaton of helium atoms to keep the temperature unchanged. This He evaporation or "shrinkage", leads to a decrease of the cross section of the droplet and the probability to collect a further particle is reduced. The involved energy is composed of the following contributions [6].

$$E = \langle E_{kin} \rangle + E_{in} + E_{binding} + E_{cluster} \tag{1.7}$$

where

$$\langle E_{kin} \rangle \approx \frac{3}{2} k_b T + \frac{1}{2} m v^2 \tag{1.8}$$

is the kinetic energy of the droplet depending on it mass and velocity and temperature in the gas cell.

At a certain energy entry, the complete droplet evaporates if to may dopping acces
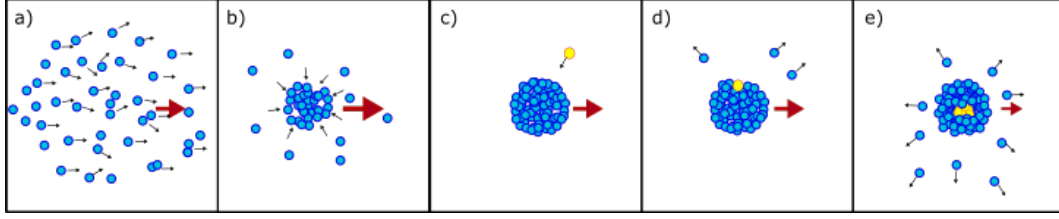
Figure 1.7: animation of the He creation , doping and evaporation. From left to rigth, we see the He droplet production; after been released by the supersonic jet, the Cluster formation, the pickup process of the dopant and finally the He srinking process.

to it. With E_{kin} the average kinetic energy, E_{in} the internal. Several studies have studied the $E_{binding}$ with ^4He, given a broth number of materials to work with.. it also importat to take into acount that the binding energy include the cluste dopant binding as well as the dopant$-$dopant relation. [60]. Acommung energy bounding for example $Xe - He$ is arround $26.9meV$ [39], or $He - H_2O$ is about $0.1eV$ [40]. A more detailed table of all the energy bounding energy used in this study can be found in the appendix.

1.1.2 Neon Droplets

Ne is the second lightest inert gas with atomic number 10, it have 3 isotopes, the ^{20}Ne with more than 90% of abundac, folloowed by ^{21}Ne and ^{22}Ne, all of them can be found stable in nature [44]. As a nobel gas, it shares most of the properties already mentioned for He, excepted for its superfluidity. It have a a quite large Ionization potential for the firs electron at $Ip = 21.56eV$, what makes it quite suitable to use with strong fields lasers, as a matrix, because at low intensities it will not interact (get highly ionized) with the laser field, so Dopants can be carried in a non interactive way.

At extreme temperature, Ne is solid as shown in the graphic ??, althougth it triple point and solidification limit allow it to be used at extream low temperatures too. Its triple point is arround $T_p = 24K$ [66] and have a rather high initial Ionization Potential.

Ne cluster also provide an ideal medium for quemichal reactions as solvation effect and heterogenius chemestry at a miscroscopic level [21]. With a proper regulated pick-up system teh reactants are deposited in a controlled way in the cluste and the cluster becomes a nanoreactor. in the same way, the low temperatures at the Ne the reactants will dicresse the ere degrees of freadom and act in a more basic and predictable reactions. [20].
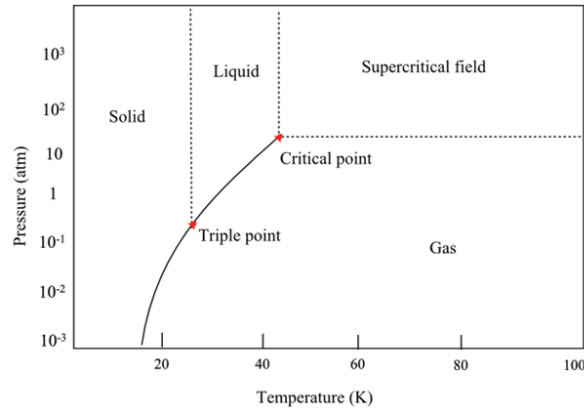
Figure 1.8: on the left. Neon phase diagram. taken from [66],on the right, $T - S$ phase diagram of Ne. The critical point is located at $T_c = 44.49K$ and a molar entropy of $S_c = 30.76J/(molK)$. The dashed lines represent regions. Taken from [8]

The conditions for creating Ne clusters are quite similar to the ones explanied above, also well explained in the famus Hagena law [26], for different temperatures and nozzels. Several studies have been realized on the characterization of Ne clusters have been achieved. One example is by *R. von Pietrowski et all*, on contrary to the He clusters, on Ne is important to work at temperatures and pressures far from its solidification point. At extream low temperatures, diferences in preasure leads to a change on the size clusters, the higher the preassure in the nozzle the bigger the droplets. As example in *Pietrowski* work,, was shown that small droplets, $N = 300$, been N the number of atom in the cluster, are in a "liquid" stade but for bigger droplets solidification is present. In addition, the location of the doppant also will be affected drastricly by these sizes changes. When the droplet is on a "liquid stade" the dopants atoms are more free to move to the center and arrond the cluster, but in a more dense droplet, this dopant will tendt to stay in the surface of the same. [47].

Same as the T-S representation of He,Fig **??**, fig **??** shows the isentropic processes as simple vertical trajectories. One advantage in this color plot (color available online) is the visibility of the two-phase region where condensation may take place. The dashed lines represent isobar lines at $p = 100, 1000, 1000, 10000,$ and $100000\ Pa$ from left to right respectively. SOn one hand, upersonic expansions which originate in the vapor phase at a very low source pressure, equivalent to a comparatively large stagnation entropy s_0, will not reach this region. On the other hand, for negative entropies the solid state is always reached and for low temperatures ad relative small entropy the liquid state is the predominant. In contrast, supersonic jet expansions which originate at high source pressures will arrive at the saturation curve. Thermodynamically, condensation is feasible at the gas-liquid phase bound-
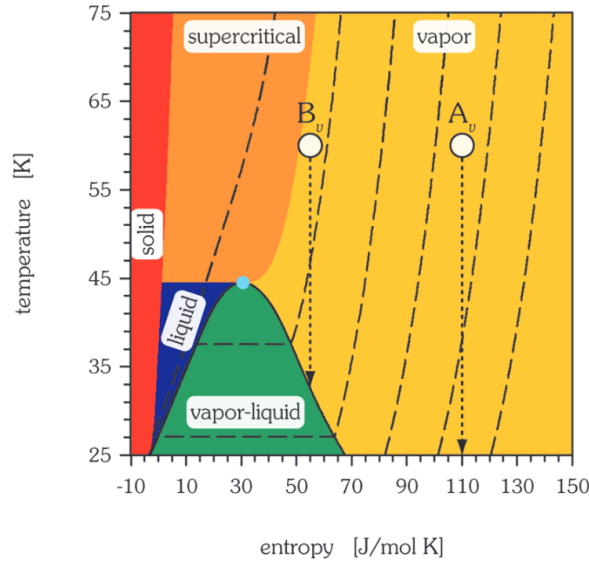
Figure 1.9: on the left. Neon phase diagram. taken from [66],on the right, T−S phase diagram of Ne. The critical point is located at $T_c = 44.49K$ and a molar entropy of $S_c = 30.76J/(molK)$. The dashed lines represent regions. Taken from [8]

ary. Accordingly, isentropic expansions reaching the binodal line (Magenta point in the peak of the Vapor-liquid phase) might be expected to yield both uncondensed particles and condensed species such as clusters and droplets. Hence, for sufficiently high pressures it is shown from this phase diagram to expect always a gaseous beam; this is irrespective of the initial reservoir temperature.

1.2 Cluster-Intense Fields Interaction

To understanding of the interaction atoms-fields have been study broadly in physics since Einstein Photoionizasion Theory [14], that gives a base on all the quantum electrodynamics theory. The basics unders this theory is the behaivour of ligth as a electromagnetic field where the electron as a bounded charge in the atom can be afected. This quantum dynamic theory is well understood since 1957 for small atoms, with one, two or few electrons [3], but still big molecules and atoms have been challenging scientific for years. In this chapter we will give a brief introduction to the photoionization process, explaining at the same time multi-photoionization and tunnelling precesses, so we can finish with a more detailed presentation of Strong field interaction with clusters and the Keldish theory.

1.3 PhotoIonization for single atoms

The process of photoionization describes the leaving of an electron from its bound state into the continuum by interaction with electromagnetic field radiation [5]. The atomic bounded electrons while going through an electromagnetic field, in our case the laser beam, can absorb enough energy to get excited and fly away from the nucleus. A bound electron only can escape from an atom by absorbing photons its energy exceeds the binding energy of an electron [14]. When the photon energy of the laser is smaller than the ionization potential of the target, the electron can absorb two or more photos in the ionization process, this is called Multi photon ionization (MPI). Another possible process is called, tunnelling ionization, where due the quantum mechanical properties of the electrons under certain conditions absorbs enough energy enough to be in an above threshold regime, due it quantum dynamic properties it can escape from its bonds via tunnelling.

There is a variety of theoretical approaches to describe the interaction of laser fields with atoms. The Hamiltonian of the system of N particles (ions and electrons) with pairwise Coulomb interactions under the action of an external time-dependent electric field has the form:

$$H = \sum_{1 \leqslant i \leqslant N} \frac{P_i}{2m_i} + \sum_{1 \leqslant i < j \leqslant N} \frac{q_i q_j}{\mid r_i - r_j \mid} + \sum_{1 \leqslant i \leqslant N}^{n} q_i r_i \varepsilon(t) \tag{1.9}$$

where r_{i,p_i} and q_i are the coordinates, momenta and charge of the particles, including the interaction between the classical electric field and $\varepsilon(t)$ where [45]

$$\varepsilon(t) = \varepsilon_0 e_z cos(\omega t + \varphi) \tag{1.10}$$

The process that drives ionization can be divided on two regimes, a quantum electrical regime and a classical one. [33]. Equation 1.9, use the non-relativistic approximation and neglect contributions from magnetic fields. The classical description of the laser field is a good approximation for intense enough pulses, otherwise, quantum electrodynamics description is necessary.

An electron in the initial level with energy E_i can absorb an photon with energy $\hbar\omega$ leading to final transition where $E_f - E_i = \hbar\omega$, when the energy of the photon is larger than the bounding energy, or the Ionization barrier the electron is free with a the remaining kinetic energy $E_{kin} = \hbar\omega - I_{pot}$ [2]. In classical mechanics the probability of the energy transition depends directly on the cross section (σ) of the electron and the field. However, in quantum mechanics, the photoionization cross section is related to the its transition probability between the initial and the final

state given by Fermi's golden rule

$$W_{|i\rangle \rightarrow |f\rangle} = \frac{2\pi}{\hbar\hbar} |\langle f|H|i\rangle|^2 \delta(E_i - E_f - \hbar\omega) \qquad (1.11)$$

$$\sigma(\hbar\omega) = \frac{2\pi}{3} \alpha a_0^2 \hbar\omega |\langle f|r_n|i\rangle|^2 \qquad (1.12)$$

When eq. 1.11 is the transition probability of one electron to jump from initial state i to final state f, where H is the Hamiltonian operator. Eq. 1.12 is the consequent cross section considering only the dipole part of the interaction Hamiltonian, where α is the fine structure coefficient, r_n is the position operator of the electron n [19].

The energy photon needed to ionize an atom, is directly proportional to the energetic distance between the electronic states and the ionization threshold. For states closer to the ionization potential a VUV photon can be enough to free an electron but for inner electrons higher photon energies are required, varying from several tens eV to the order of several tens of keV, needing radiation sources at shorter wavelengths such as XUV to X-rays. [2]

After photoionization is done, the electronic structure of the atom needs to rearrange via, due to the vacancy left by the ejected electron. Two relaxation processes can happen during this time. An electron from the outer shell will decay and replace the freed one, therefore the energy difference of the needs to be released in the form of a fluorescence photon or Auger electron. On one hand, in case of a fluorescence decay the ionic state of the target does not change, since no additional electron is released. On the other hand, the Auger decay is a non radiative relaxation process, where a second electron is released from the Coulomb potential of the ion.

In example. As shown in fig ??, if an photon with energy $\hbar\omega > E_{bin}$ ionized an electron, this will leave the atom lifting a gap. An electron in the higher levels will replace the outer one, leaving an excess of energy. The outcome will be a fluorescence process with $E_{flu} = E_{in} - E_{out}$ or , the Auger $e-$, if $E_{in} - E_{out} > E_{bond}$ and this electron can also escape the atomic Coulomb potential [53].

1.3.1 Multhiphoton and tunnelling Ionization

Ionization is also possible even when one photon energy is lower than the binding potential. Laser fields with intensities below $I \leqslant 10^{14} W/cm^2$ are not strong enough to change the binding potential of an atom significantly [51] and is when multiphoton Ionization takes place (MPI). MPI is the simultaneous absorption of several photons to overcome the ionization barrier. The way MPI occurs depends on the laser
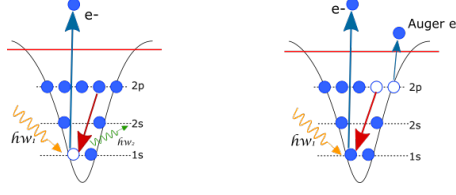
Figure 1.10: two example on the relaxation processes. On the left, A photon ionized an electron and the Electron E_{in} replaced, expelling a fluorescent photon in the process. on the right, the energy released by the replacement electron is enough to make another electron in the outer shell to also go to the continium, Auger electron. Taken form [50]

frequency and intensity. When the intensity is much lower than the characteristic atomic resonance, MPI occurs via transitions through virtual states. Ionization by several photons at low laser intensities can be realized by the so-called resonance enhanced multiphoton ionization (REMPI) [42]. Ionization by a REMPI process takes place in two steps First, a resonant excitation by one or more photons takes place on an electron state of the atom. In the second step, this electron state is transformed into a virtual state, to an upper state until the electron is excited by spontaneous decay. So for example the total energy absorbed by an election until it gets ionizes is $n * \hbar\omega > I_{pot}$ where n is the number of photons absorbed until it actually have enough energy to overcome the potential I_{pot}

For Laser intensities $I > 10^{14} W/cm^2$, higher intensities and lower frequencies, tunneling ionization (TI) is more likely to occur. In this case, the binding potential of the atom get is strongly affected by the electric field of the laser. Around the peak of the electric field the potential gets narrower, and the electron in the outer states get closer to the bidding barrier, allowing the electron to tunneling through the confining potential to the continium [23]. TI is inherently a quantum process. The bending of the Coulomb potential becomes by the superposition of the coulomb potential and the laser field. Therefore TI must occur when the time of the ionization is shorter than a laser oscillation cycle [5]. Based in the same principle, when the Laser field becomes so strong to lower the binding potential that separates the highest electron level, then the electrons in this state become free electrons. This process is called barrier suppression ionization or BSI [37].

In the fig **??**, we present a sketch of the 3 possible ionization processes explained above. On the left we present a simple ionization process where a photon with energy $E_{phot} = \hbar\omega$ is higher than the potential barrier. In the center a MPI process is shown, n photons excite the inner-shell electron, exiting it through virtual level until it finally has enough energy to be free to the continium. Finally, on the left a TI happens. Here the coulomb potential barrier is affected by the laser files bending,

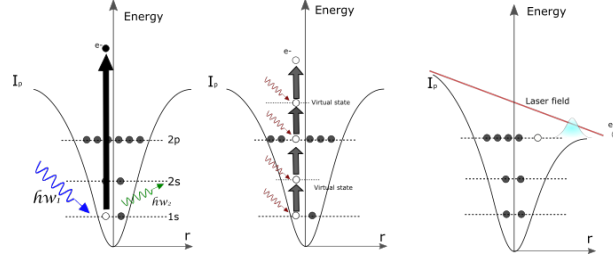the outer shell electron gets closets to it until it tunnels [50].

Figure 1.11: On the left is the sketch of a single photon ionization process, where a photon with energy $E_{phot} = \hbar\omega$ is higher than the potential barrier I_p. On the center the MPI process, inner-shell electron absorbs n photons, getting excited through the electronic levels (reals or virtual) until it reaches the continuum. On the left the BSI Process, the coulomb potential barrier bends by the laser fields, been lower than the outer shell electron state, the electrons can scape easilly. based on [50].

As explained the Intensity of the external field plays an important role in the ionization process. A rather easy way to differentiate when each process needs to be taken into account is provided by the Keldysh parameter [34].

$$\gamma_k = \sqrt{\frac{I_p}{2U_p}} \tag{1.13}$$

Where γ_k is the Keldish parameter, I_p is the atoms ionization potential and U_p is the ponderomotive potential defined as:

$$U_p = \frac{e^2 E_0^2}{4m_e \omega_0^2} \propto I\lambda^2 \tag{1.14}$$

where m_e is the mass of the electron, ω_0, λ, I and E_0 are the frequency, wavelength, intensity and the peak of the electric field of the laser pulse. On one hand, when the Keldish parameter is higher, $\gamma_k \gg 1$ MPI regime is considered. On the other hand, the $\gamma_k \ll 1$ describes the TI interaction.

1.3.2 kelysh Theory

In this section we will give a brief introduction to keldysh theory and the main repercussions for our work as the ionization rates. We were based this subchapter in the work of Keldy et all, [34], and the papers review of the theory by [48] and [33]. For a deeply explanation we recommend the reader to reference this works.

The keldysh Theory, also known as the Keldysh–Faisal–Reiss theory (KFR), is well used for the description of quantum process induced by intense laser radiation. The

applications and advantages of Keldysh formulation in many-body theory among can overcome from, treatment of systems away from thermal equilibrium (with or without presence of external fields), solutions in super symmetry methods of systems with quenched disorder to the calculation of the full counting statistics of a quantum observable [31].

According to the Keldysh Ansatz, the transition probability amplitude between an atomic bound state and the continuum by the value of the photoelectron momentum p measured at the detector is given by: [48].

$$M_k(p) = -\frac{i}{\hbar} \int_{\inf}^{+\inf} \langle \Phi_p \mid V_{int}(t) \mid \Phi_0 \rangle dt \tag{1.15}$$

Where M_k denotes the Keldys transition probability, Φ_0 is the bond state wave function unperturbed and Φ_p is the canonical momentum, equal to p, also known as the Volkov Funtion, and V_{int} is the electron field interaction operator. If the amplitude of ionization $M_k(p)$ is known, the differential probability to find the photoelectron in the elementary volume near the momentum p is given by the momentum distribution of the photoelectrons

$$dW(p) = \mid M(p) \mid^2 d^3p \tag{1.16}$$

Giving a total probability of

$$W = \int \mid M(p) \mid^2 d^e p \tag{1.17}$$

Meaning that, for enough long pulses, containing a large number of optical periods so that its electromagnetic field is close to a periodical function of time close to the initial, it is physically more appropriate to use probabilities per time unit (rates) instead of time-integrated values.

1.3.3 Ponderomative energy

As soon as an electron is released into the continuum, it is under the influence of the external laser field. A description of the energy that it acquires during this interaction is given by the ponderomotive energy (PE).

$$U_p = \frac{e_2 E_a^2}{4m\omega^2} \tag{1.18}$$

Where m and e is the electron mass and charge, E_a and ω_0 amplitude and frequency of the electric field respectively. The formula of the ponderomotive force can be easily derived as shown in [49] [9]. Let's consider a polarized electric field (in

a.u).

$$E = \hat{z}E_a sin(\omega_0 t) \tag{1.19}$$

Considering only the $\hat{z}$-components so we can avoid the vector sign. By classical mechanics we have.

$$p(t) = -\int_{t_0}^{t} E(t\prime)dt\prime = \frac{E_0}{\omega}(cos(\omega_0 t) - cos(\omega_0 t_0)) \tag{1.20}$$

The term on the left of the parenthesis is known as the time varying Quiver terms, and on the one on the right, reefers to the drift motion. Expressing the fields in terms of vector potential we will have

$$E(t) = \frac{\delta A(t)}{\delta t} \tag{1.21}$$

$$p(\infty) = A(t_0) = -\int_{-\infty}^{t} E(t)dt = \frac{E_0}{w}cos(w_0 t_0) \tag{1.22}$$

in the case where the pulse duration is big $t \longrightarrow \infty$ the $p + A(t) = 0$. This means that the momentum acquired by the electron will depend on the phase it is realized wt. Since the electron can be unbound in any phase of the laser pulse, will have an average kinetic energy described by

$$U_p = \frac{1}{2\pi}\int(-\frac{E}{w}cos(wt))^2 d(wt) = \frac{E_0^2}{4w_0^2} = \frac{p_{max}^2}{2} \tag{1.23}$$

The pondemorotive energy also gives the maximum momentum that an electron can acquire (eq. 1.22), given at the maxima. The ωt phase relation, defines what it called*the three step model* showed in figure 1.12 . The first step corresponds to $\omega t < \pi/2$ where the laser field is suppressed, and as explained above, TI or BSI can take place. The second step, is where $\omega t > 3\pi/2$, on contrary step 1 the potential barrier is enhanced, electrons in the continuum that was winning kinetic energy are caught by the potential again, being driven back to the atom. Finally the step 3 at phase $\omega t = n * \pi$, for $n01, 2, 3....$ At $n = 2$ it is called "recollision process" of the electron. Where the electron can be caught by the potential again, and the excess of energy release another bound electrons, depending on the kinetic energy necessary [36]

If we transform the eq. 1.23 to laser intensities we will have $U_p = 9, 33*10^{-14}I[W* cm^{-2}] * \lambda^2[\mu m]$. For a MIR-pulse with intensities $\sim 10^{14}[W/cm^2]$ and $\lambda \sim 3200[nm]$ we have electron energies between one and a hundred of eV.
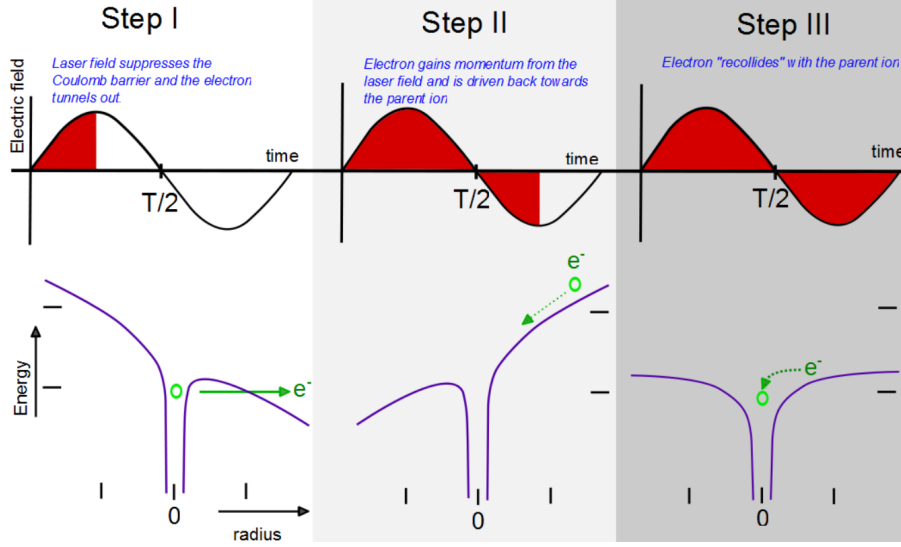
Figure 1.12: Recollision process at the three step model. Taken from [37]

1.3.4 Cluster Ionization

Until now, we have shown one of the most known ionization processes for single atom. But on cluster ionization, the dynamics are quite different and need a bit more detail. Clusters are combinations of atoms or molecules which, depending on their species, are held together by Van der Waals forces, ionic bonds or metallic bonds. In this explanation we refer only now and on to He cluster, which mainly are just affected by Van der Walls attraction. The investigation of clusters is of scientific interest in many studies, a cluster can be generated in a wide range of sizes (10^2 to 10^7) [56], having a radius significantly smaller than the MIR laser pulse wavelength used on them, meaning that all its atoms are equally affected by the pulse filed, in other words it penetrates all over the cluster.

The first problem that He cluster faces is auto-ionization. Being a rare gas, its ionization potential is higher than many of its doping molecules used. For example, under MIR lasers He clusters need $I > 10^{15} W/cm^2$, so TI or BSi is not the main process at beginning of the plasma generation. Other interactions have to be explained in order to describe the process properly. This section we will be based on *Saalaman et. all* work [52] and *Grüner et. all* [24], for this purpose, we will divide the process in three phases or stages.

The first stage, called *"atomic ionization"*, the doping atoms are ionized independently of each other by the electric field at the leading edge of the laser pulse, it occurs mainly through inner ionization, especially on TI or BSI. The resulting free electrons acquire positive kinetic energy and have two options, leaving the cluster or they stay inside the cluster attracted to its positive ion core. After the first stage, the

cluster nanoplasma is *ignited*, consisting of ions and quasi-free electrons, electrons that are free to travel inside the cluster volume but still not into the continuum [38].

The second stage is the *nanoplasma expansion*. During this stage the cluster is still interacting with the laser field, acquiring, by a large number of processes, energy in atoms and electrons. Ions are further created by a combined force of the laser and other ions, the *ionization ignition* [24]. Quasi-free electrons oscillate, driven by the laser pulse and are heated to high temperatures. The heating becomes extremely efficient when the collective oscillations of quasi-free electrons become resonant with the laser pulse, Triggering a cascade reaction to more outer ionizations, freeing the remaining electrons in the cluster, this process is called *plasma resonance* [52].

After the laser pulse is over, the last stage starts. The ions continue to expand, in consequence, the radius rises as same as its cluster potential becomes smoother. So, it is easier for the highly energetic quasi-free electrons to leave the cluster, forming a coulomb explosion that destroys the cluster in a beautiful ions-electrons cascade. This process was first describe by *Ditmire et. all* [13] combining high energetic collisions with cluster resonance absorption.

The graphic ?? shows on the left how the cluster potential is composed by the Van der Walls potential and atomic forces of the different atoms that compose the cluster. On the central images, additional to the atomic biddings, the electrical force due the ions in the cluster increase the potential, the laser pulse is still on and the quasi-free electron will gain energy while they are in this. Finally, on the right the laser field is off, the electrons have fled away and the cluster ion have been repelling each other so the potential is reduced to the minimum(just atomic interactions.)

1.3.4.1 Cluster expansion

Depending on the droplet size and the laser intensity, the Cluster can expand in two different ways. If the laser intensity is rather high and the droplet is small, a Coulomb explosion can occur. On the contrary, if the laser is not intense enough or the droplet is too big, a nanoplasma can be generated, therefore an hydrodynamic expansion will take place. Two forces are really important during the cluster expansion. Both act on the cluster during the phase two and three(during and after the laser pulse). The first, is the force associated with the free electrons with high kinetic energy. These hot electrons expand and pull the low energetic electrons and heavy ions on its pad [13]. The other force acting on the cluster is due to the inner cluster charge itself. The hottest electrons in the cluster will have a mean free path large enough so they can free stream directly out of the cluster, and, if the electron's energy is large enough to overcome the space-charge buildup on the cluster, they will leave the
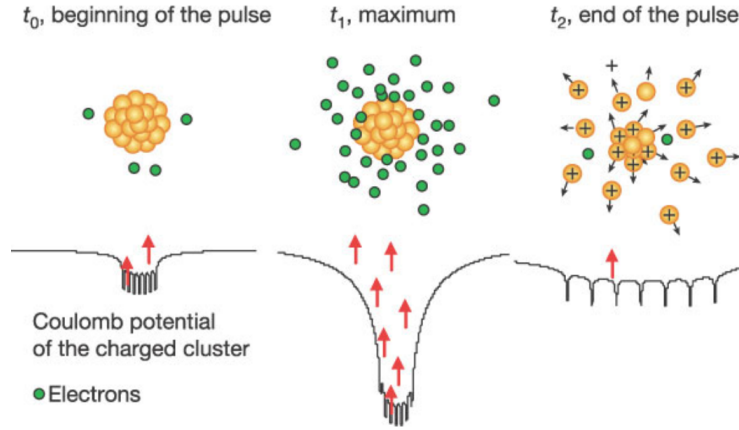
Figure 1.13: Cluster potential regimes. On the left, the atomic ionization starts the plasma formation. On the center, The quasi-free electrons auto-ionize the cluster, increasing the potential barrier and gaining energy due the laser field so a coulomb explosion can take place. On the right, The Coulomb explosion is finished, the potential is driven to it minimum and all the electrons and ions are ejected. Taken from [62]

.

cluster altogether. If the charge buildup is sufficiently large, the cluster will undergo a Coulomb explosion [29]. According to Madison et all, a time scale for the laser pulse duration where the coulomb explosion can take place should be closer or lower to the femtosecond regime, depending on the element composing the cluster. [41]. Based on the laser power available on modern laser pulses, the same studies present that electron after a coulomb explosion can get kinetic energy up to 6KeV.

When the intensity is not enough to make the atomic bonds to break, the electrons remain in the cluster forming a hydrodynamic expansion as a result of a conversion of electron-thermal energy to direct kinetic energy [17]. The effects that the expansion has on the electron temperature can be calculated by equating the rate of change of radial kinetic energy from the thermal contribution with the rate of change of thermal energy within the cluster. When this condition is fulfilled. The electron can present a resonance condition in the cluster, traveling in the space-charged forces formed by the plasma, winning enough kinetic energy until all the system collapse.

Although the two models are different in each regime, for example, at low kinetic energy or the beginning of the pulse, the Coulomb explosion produces less ions for low energies compared to the product on hydrodynamic explosions. Further, the number of high energy ion the coulomb explosion can create (although in less quantity) tent to be hotter ions too. We have to take into account that even the two processes are described for different laser regimes. Both processes can happened in parallel, but at certain energies is clear, that one or the other will be the responsible
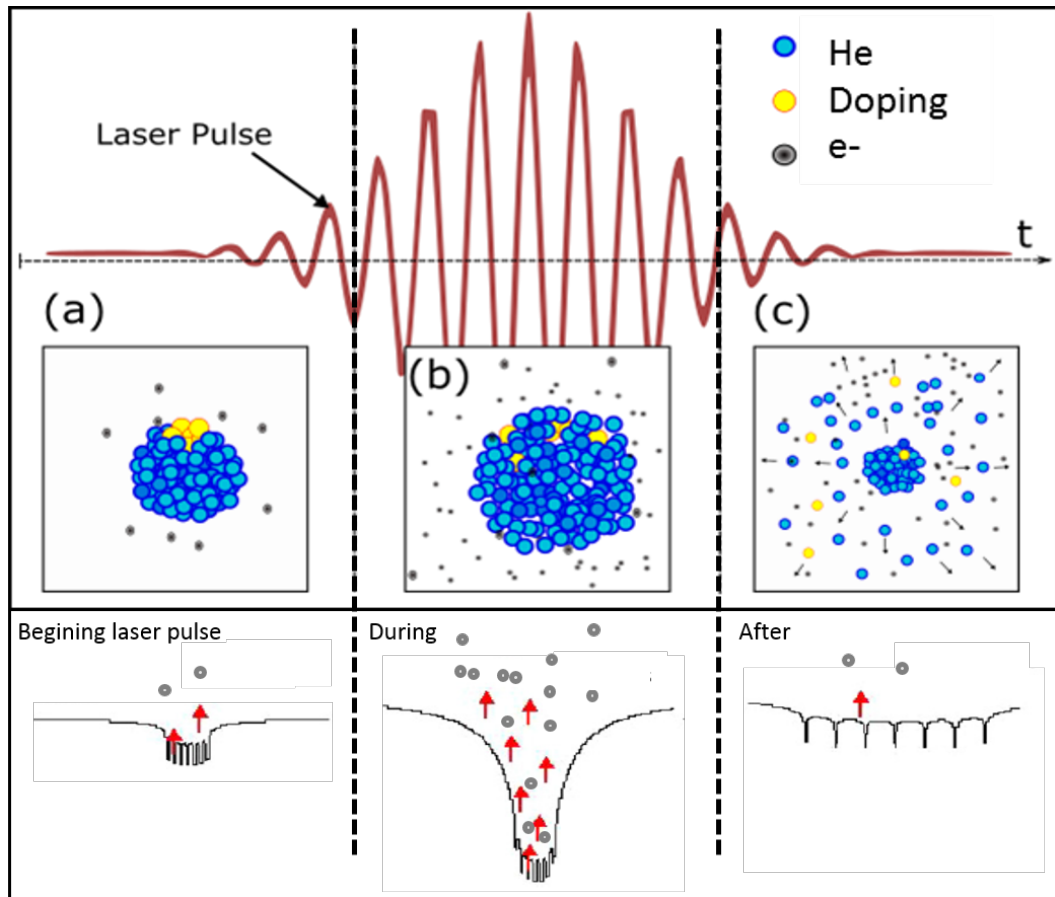
Figure 1.14: sketch of the Coulomb explosion for a doped cluster due the excitation of a pulsed laserfield. At the beggining of the process the laser ionized the droplet, until some femtoseconds (up to 500fs) after, the system colapce and result into a coluomb explotion.

at the end, for the collapse of the system.

1.4 VMI spectrometer

A Velocity-Map-Imaging or VMI spectrometer is used to investigate velocity distributions of charged particles, which are generated in a defined volume, typically by photoionization. The distribution of the particles, on the other hand, should be the object of the measurement and therefore also have an influence on the results. A laser generates charged particles by photoionization in the interaction region, which are accelerated by means electric lens created by two electrodes. Typically, this is a system consisting of an Microchanel plate or MCP and a phosphor screen, which is observed by means of a CCD camera on top. Electron or Ions are created from the atomic photoionization, these particles are accelerated by an applied voltage and generate further electrons. Once these arrive to the MCP an electronic avalanche occurs, been able to detect even single electrons. The electrons hit the phospho-screen igniting photons that a focussed CCD camera can detect. The VMI used in this experiment satisfies this requirement is the Eppink-Parker-Design [16], the lower electrode is called Repeller followed by the extractor, ground electrodes and a E-lens before hitting the MCP array. All electrodes have a circular layout and are about $1mm$ thick. The extractor and ground electrodes have a concentric hole where the particles pass through.

1.4.1 Velocity distribution in VMI

Based on the assumption done above where the VMI, we assume that the charged particles come from a point in space emitted between the Repeller and the extractor. Furthermore, we presume that the energy generated by the excess kinetic energy of the particles obtained during the ionization process, small in comparison to the is the energy they receive from the electric field. The initial conditions of the charged particles are determined by the ionization volume and the initial velocity vectors $v_i = (v_x; v_y; v_z)$, whose distribution is to be measured. The particles are measured by the E-field in the direction of the spectrometer axis of the planar detector surface Where they accelerate, depending on their initial velocity vectors. If one starts from an isotropic initial distribution of the velocities, particles with differing initial velocity vectors can finish in the same point on the detector, as shown in fig **??**. This results in a loss of information due we are trying to get some data of a 3D space from a 2D projection.

Figure 1.15: Representation of particle trajectories A, B and C of the ionization volume to the detector plane, which, in spite of initially different velocity the finish on the same point of the detector plane. Withdrawn from [?]
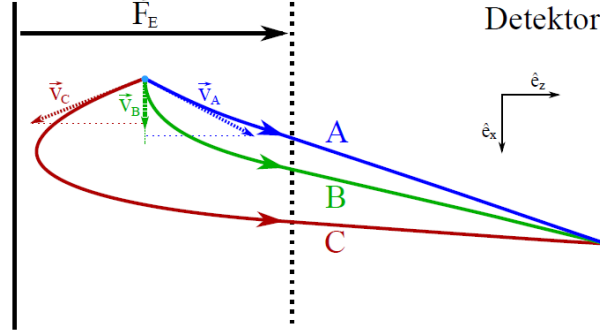
Assuming a cylindrically symmetric distribution $f(r, y)$ along the y-axis. If an infinitely far away observant look at the distribution F along the z-direction. He sees the integrated (along the z-axis) sigma With a basic axis conversion it can be shown that along the Z direction, the projection of the distribution F of the integrated signal respond to.

$$F(x, y) = 2 \int_{|x|}^{\inf} \frac{f(r, y)r}{\sqrt{r^2 - x^2}} * dr \qquad (1.24)$$

Been F in cylindrical coordinates and $r^2 = x^2 + z^2$. Also called *Abel-transform.* But in order to resolve or signal we need the opposite procedure, turn this 2d distribution into the 3d spherical distribution that we assume in the beginning. For this process is called *Inverse Abel-transform,* and it can be shown as.

$$F(r, y) = \frac{1}{\pi} \int_{|x|}^{\inf} \frac{dF(x, y)}{dx} \frac{1 * dx}{\sqrt{r^2 - x^2}} \qquad (1.25)$$

The main problem that carries this transformation is that is not resolvable to a non continues distribution, that is the case of the Images recorded by the camera. So a numerical method needs to be used. Fortunately, a Software Pbasex, is available to solve this integral. The idea is to have a basis function f_k (in this case Lagrange polynomial) in the space of distributions f. Their projections F_k onto the detector are well known, and the Able transform will be set as:

$$F_k(x) = 2\sigma \rho_k(x) \{1 + \sum_1^{k2} \{(x/\sigma)^{-2l} \prod_{m-1}^{l} (\frac{(k2 + 1 - m)(m - 1/2)}{m})\}\} \qquad (1.26)$$

If every measured image can be expressed in this basis, then the reconstruction

of the F distribution when $k \to \text{inf}$ can be obtained. A graphical example of this transformation is given in fig **??** where each color represent a f_k projection, where all f are in the same basis, the sum of all the different f will set the final reconstructed F_K.

Figure 1.16: At the top of the graphic some basic functions f_k in different colors, which can be used for the Inverse-Abel transform in the BAsex method. On the bottom, the corresponding Abel-transformed functions Fk. Taken from [?]
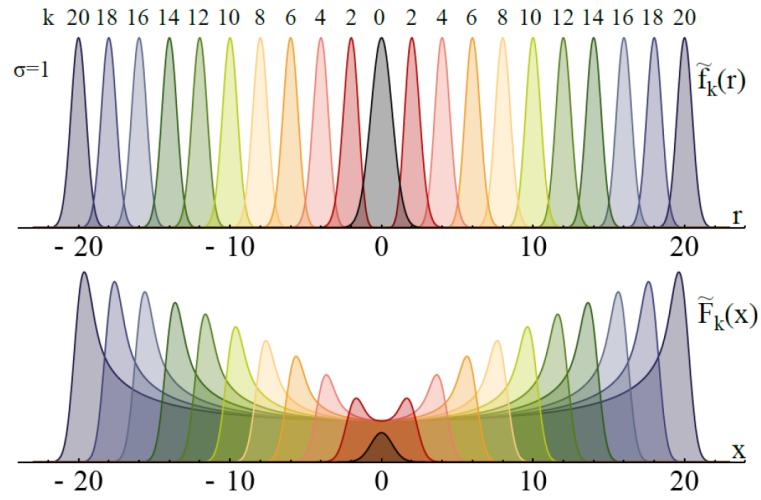
2 Experimental setup

In this chapter, we will present the experimental setup used, giving special attention to the Nanodroplet generations, the doping process and the data acquisition system. A sub-chapter is also dedicated to the single shot correlation data acquisition system tested specifically for this Master's project. The apparatus we worked with, is part of the group of Molecule and Nanophysics at the University of Freiburg, Germany, and was calibrated and used for the experiments in [54] and [30].

In figure?? a sketch of the apparatus is shown. From left to right; The source chamber where the ultra cold molecular beams are produce. The central chamber or "doping chamber", where the beam gas is doped via pick up process using a gas doping cell or a diffuse oven for alkaloids, where gases or thermally vaporized solids are used as dopants. The last chamber or "detection chamber", combines a VMI - TOF detection system and a Langmuir Taylor (LT) detector. To generate the nano plasmas, the apparatus was used in two different institutions, at the Max Plank Institute for Nuclear Physics in Heidelberg and the Extreme light institute (ELI) in Szeged, Hungary, because of the special laser systems that can be provided in there.

The following sections describe the essential components of the apparatus, taking special attention to the new Triggering systems implemented to correlate the VMI and TOF signals. The structure where compacted to a length of about 240 cm long, each chamber has attached to its own turbo pumps with pre-vacuum scroll pumps and separated by valves and skimmers. On one hand, this enables to manipulate the vacuum in an independent way and control the targets in the "detection chamber". On the other hand, allows an optimum adaptation of the suction power of the pumps to the gas load of the individual chambers as wheel as to ventilate and open, without having to disturb the entire system.

2.1 Source chamber

The Source chamber consists of a 6-way CF vacuum chamber, with a 2-stage cryostat power a cold-head that can be cooled down to 9K, located at the entrance of the chamber, parallel to the floor with an attached conical nozzle for the gas ex-
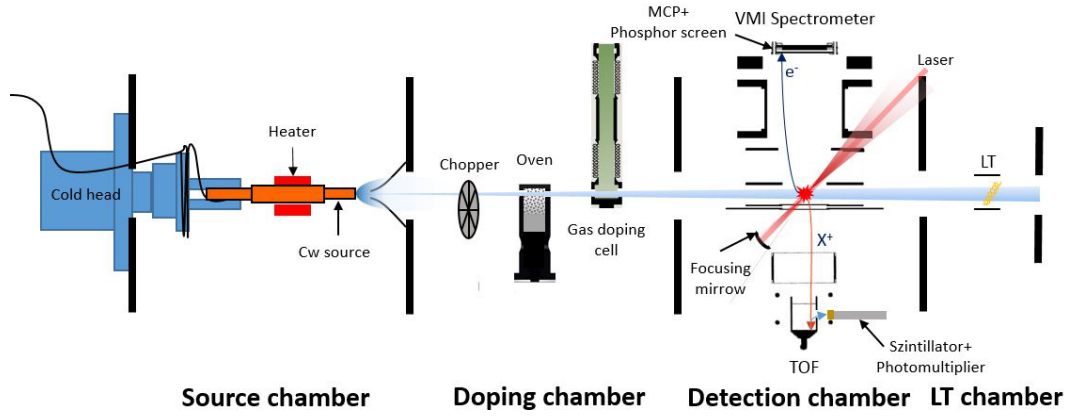
Figure 2.1: Sketch of the vacuum chambers, including the main parts of the setup

pansion process. The cooling capacity of the cryostat consists of a copper tube, into which pre-cooled helium is introduced. It can be adjusted by operating two heating resistors in combination with a sensor diode for temperature measurement and a PID controller. Controlling the resistor current the temperature at the end of the nozzle can be keeping it stable. The conical nozzle used to generate the atomic beam is the standard used in the research group on Nanoplasma research directed by Prof. Frank Steankeirmeyer at Freiburg University. It is made of copper and has a platinum plate on front with a hole of $5\mu m$ of diameter for He experiments and $15\mu m$ for Ne gas clusters. The diameters where choose in order to follow the size dependence of the $Hagenas$ "law", which together with the adjustable gas pressure and the nozzle temperature regulates the flow. The cold head-nozzle arrangement are connected to the chamber via a self-made x-y manipulator, with a thermally insulating rubber ring, which allows a beam adjustment in relation to the other components in the setup without breaking the vacuum. At the bottom of the chamber an "Agilent" turbo pump of $1800L/s$ capacity is attached to a pre-vacuum scroll pump as exhaust. A skimmer with a diameter of $400\mu m$ is located in front of the effusive jet, sorting the gas beam not just by size, but also by its velocity vectors and allowing just those beams with direction to the further vacuum chambers. To adjust the nozzle optimally to the skimmer, it is connected to an x-y displacement unit and can be aligned from outside the vacuum chamber. To prevent the small opening of the nozzle from clogging over time, high-purity helium 6.0 (99.9999% purity) and Ne 5.0 (99.999% purity) is used and can also be used outside of the measurements ensures a constant gas flow through the nozzle. At this extreme temperature this prevents that any impurity in the gas bottle can condense, blocking the nozzle or changing the conditions of the clusters production.

2.2 Dopping chamber

As explained in the chapter above, the Doping takes place by inelastic impacts with atoms from the gas phase, referenced as the pick-up technique. In this experiment we doped with both metals and noble gases, and two different methods of doping are used: Metals are heated in evaporated phase in the oven, while gas dopant yield in a Gas doping cell entered the vacuum chamber through a needle valve. On the next section, we will explain the elements of the doping chamber and its most important characteristics used.

The oven chamber is connected after to the Source chamber via the skimmer, it is also a 6-way CF vacuum chamber, with a turbo pump on the bottom, connected to its own pre-vacuum scroll pump. On the sides the flanks allow a cold trap not used in this experiment, on the other side the flank that permit connection to the oven and the vacuum sensor. The Skimmer is made of Nickel, a very thin metal easy to bend, so in order to prevent strong pressure differences in the chamber that can modify the skimmer, a bypass is connected between the two chambers using a stainless steel flexible hose. An internal stand is welded to the front of the chamber and aligned with the skimmer. This stand supports the Chopper, the gas doping cell and the oven. In the front the rail the choppers is located. It is a steel disk with three notches uniformed located, two photocells around the bottom of the disk reads the position of the bottom notches so the upper one can be positioned right in front the skimmer. In this way, when the disk rotates the beam can pass or its block by the disk in a controlled way.

After the chopper, there is the Gas Dopping cell, a circular flat metal base with a self modified KF hose. The base of the cell has a matching pattern so the hose can be easily put and remove without losing the alignment. The stainless steel flexible hose has two $5mm$ hole (one in front and one opposite to it, some cm up the base) aligned to the skimmer so the gas bean can go though. The hose is fixed to the base and goes to the top of the chamber where it is connected to a "swaglog" needle valve that allows to control the gas flux for doping the beam. A Pfiffer CMR375 Capacitive sensor is located after the needle valve so a better control of the pressures and the number of dopant in the cluster. The bendable construction allows, not just to remove the doping cell without difficulty, but also to fit it on the top without depending on a fix way to locate the top plank, in this way there is room for maneuver and the installation is faster.

Finally, at the end of the rail lies the Oven. As shown in fig **??** the oven consists of a patterned base (similar to the gas cell) that can move a few mm on $x-y$ plane. Over it, a metal cylinder with 4 heating cartridges holds a movable crucible in the

center that contains the dopant sample, this movable container is set down by a rod that comes from the top of the chamber after a valve. Both, the stove and crucible have holes (a conical entrance of $40mm$ diameter and $3mm$ diameter respectively) that allows the pass of the gas beam and are aligned to the beam pad, in this way the passing Atomic beam takes dopants via collisions with the vaporized sample material.
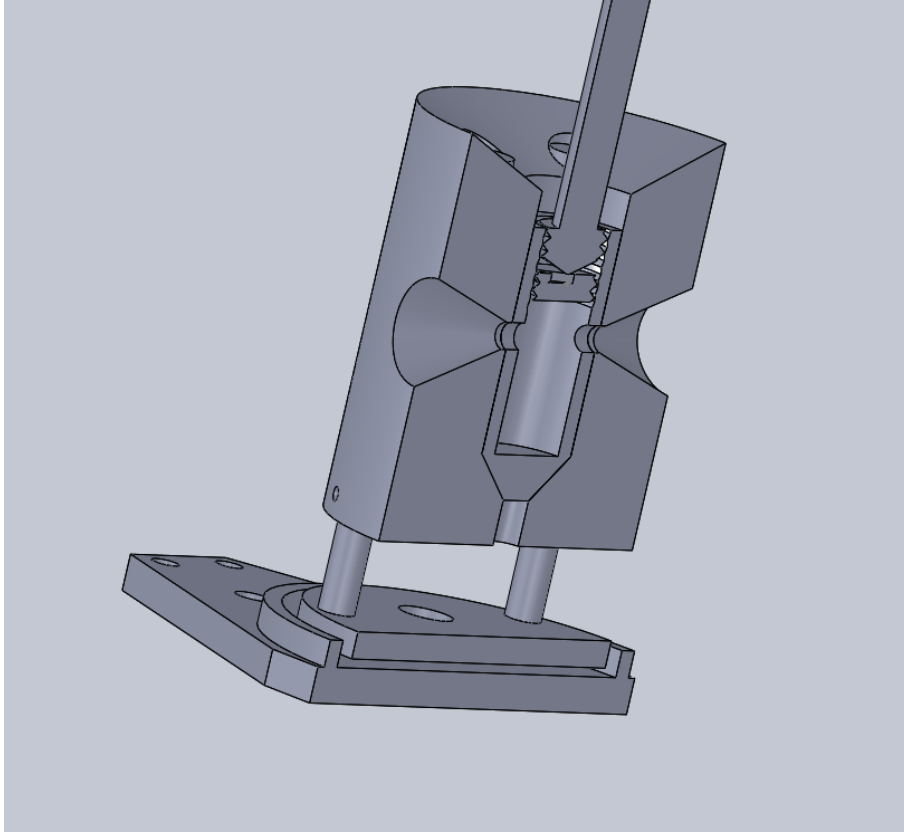

Figure 2.2: Cut of the Oven design, including part of the rod and the crucible.

One important advantage of this new oven design done by *Dominic Schomas*, is that the dopant can be change with out braking the vacuum, it was tested in this experiment and prove to be useful in saving time and effort. To control the temperature of the oven a temp sensor is fixed in the stove, and the resistors current is manage by a PID controller allowing a stable temperature during the experiment. The maximal temperature reached was $450°c$, enough to create the gas phase for the potassium K and calcium Ca used in this experiment. Finally, there is an extra skimmer of diameter $2mm$, fixed to a valve between the connection of the doping chamber and the detection chamber that helps to avoid the disperse beams or an overflow from one chamber to the other.

In addition to the doped gas nano droplets, effusive gas is also released from the

VMI	Repeler	Extractor	Lens
X1	-2430	-1940	3500
X3	-7290	5820	10500
Ion	2430	1940	0

dopant chamber into the detector chambers through a "swarlog" needle valve" and can be ionized and detected there. This disperse gas was pouring in directly on the chamber or filtered by diffused atoms going out of the oven and passing across the second skimmer once the choppers is close. This atomic gases were added for calibration of the detectors and background reduction allowing just one gas at a time.

2.3 Detection chamber

As mentioned, the detector chamber is connected to the Oven chamber through a valve and a skimmer. The detector chamber contains a newly developed Velocity-Map-Imaging Spectrometer on top, a time-of-flight mass spectrometer on bottom and a LT detector in front. In this section we will give a brief presentation of the VMI and the TOF used for this experiment, taking special interest in the new Triggering process that allows to detect single nanoplasma explosions.

2.3.1 Velocity map imaging VMI

The VMI detector used in this experiment is detailed in [54], this construction basically follows the standard geometry of Eppink and Parker [16]. It is composed by three electro lenses (Repeller, lens and extractor) that focuses the ions or electrons on a $86, 6mm$ (effective area) diameter Micro channel plates (MCP) arrange. This detector set is basically two MCP's superposed, rotated to each other and a phosphoscreen (PS) layer of same diameter facing the top plank of the chamber with a Ca-fluoride glass of $1mm$ thick. An external CCD camera is focused to the PS.

The voltages applied to the MCP and PS determine the brightness of the final pictures of the ions, so in general just one set of voltages has been used, around $1400V$ for the MCP and $4000V$ for the Ps. The achievable energy acceptance for this stack is $34eV$ for a the VMI setting 1 and $270eV$ for the X3 settings. The VMNI have a resolution of $\triangle E/E \leq 4\%$ [54]. The camera used in the experiment was a Basler acA1920-155um focused on the PS.

On fig ?? we present a view of the model of the VMI used in this experiment, From bottom to top, the structure of the electrodes consists of two Repeller electrodes
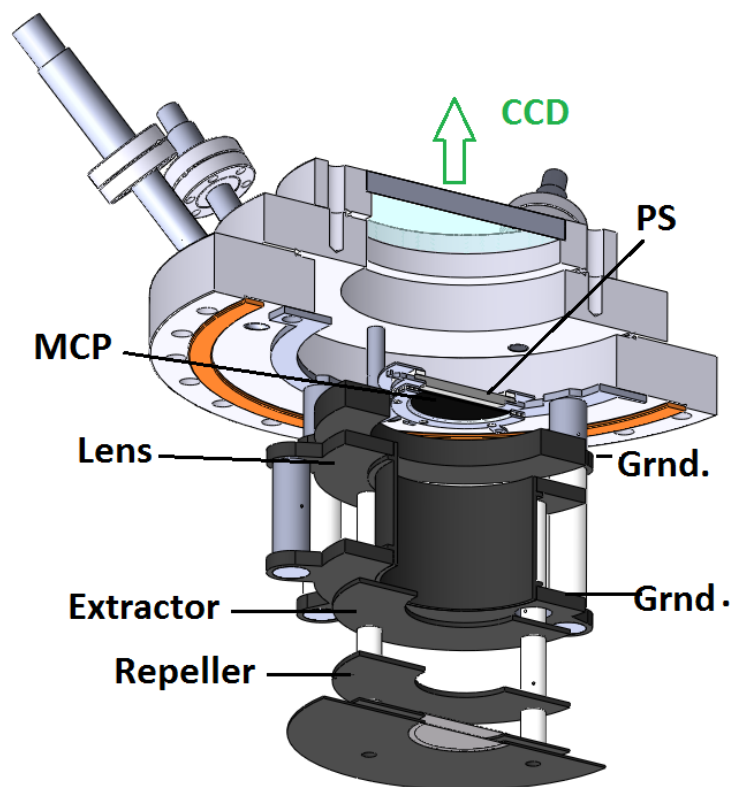
Figure 2.3: Sectional cut view of the CAD model of the spectrometer setup. On black the electrodes and the white the Polyether ketone (PEEK) isolators. On orange, the cooper ring and on blue the top window facing the CCD camera

separated by a few millimeters with circular openings on which a fine mesh copper grid is applied, an aperture electrode as Extractor, another aperture electrode which is held at ground potential and then from the extended lens electrode with the following second ground electrode. At the top, the MCP-PS arrange (on black the MCP and on gray the PS) facing the center of the window installed in the top plank of the chamber. Around the window there are three connections that allow the voltages for the electrodes and the cables are carefully arranged around the structure to avoid discharges or even disturb the uniform electric field.

The openings of the Repeller (at the bottom in bluish color) electrodes allow the use of these electrodes as well as extractor electrodes for a TOF spectrometer. In simultaneous operation of the VMI and the TOF spectrometer, the glued grids prevent mutual field effects of the two spectrometers. The Repeller and extractor are grade 2 titanium and the lens is stainless.

2.4 Time of flight spectrometer

The Time of flight (TOF) spectrometer used was based on the design by Wiley and McLaren [65]. As its name refers, the TOF mass spectrometer relates the time that a particle at an electric field requires to reach certain distance with its mass, when atoms and molecules are photoionized, they pass through an electrostatic acceleration field and are registered in a detector after crossing a field-free flight path. Based on the flight time the ratio m/q of a particle can be determined as:

$$t - t_0 = a\sqrt{\frac{m}{q}} \tag{2.1}$$

Where a is an experimental factor depending of the flight distance, electric fields and material of the setup, m/q is the relation mass - charge, t_0 is the time ionization time (given by the laser)and t is the time of flight.

The ions creation takes place in the aperture between the Repeller and extractor electrodes. Behind the extractor electrode there is a further aperture electrode, which is held at zero potential and thus generates a pre establish flight route with a defined field, grids are glued to the openings of the electrodes to prevent the propagation of the fields through the orifices in the electrodes. The Repeller electrode is set to a positive potential and the extractor to a negative potential. The resulting electric field accelerates the ions through the openings in the flight tube, on which grids mount on both sides keep the drift path free of field. Once the coulomb explosion takes place, the ions are accelerated by the electric field of the Repeller and then fly through a field-free drift path to the detector. This allows a complete mass

spectrum to be recorded within a few microseconds in a single measuring step [43].
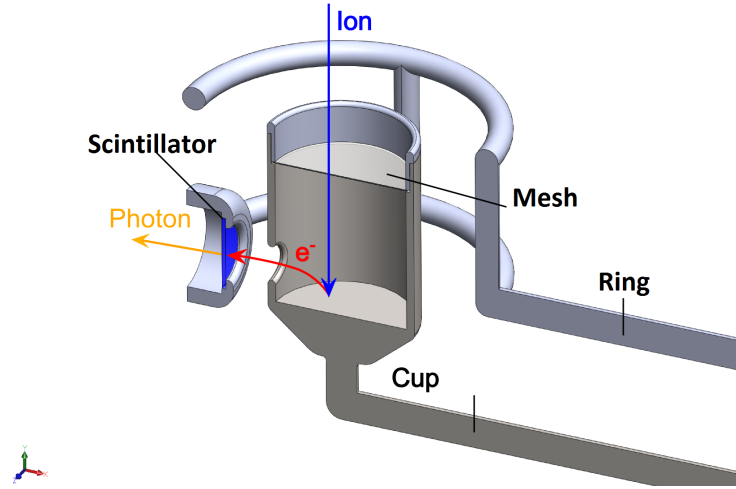

Figure 2.4: Illustration of the functional principle of a Daly detector.

The flying Ions finally are detected by a Daly detector [10]. It consists of a cup, a grid and a ring. The cup lies on negative high voltage while the ring for positive. The ions from the Repeller pass trough the field free tube corrected by a drift electrode. Since in the direction of the hole the potential for electrons drops sharply, the ring electrode generates an electric field, which directs the ions into the cup. The ions that pass the grid at high speed hits on the bottom of the cup, they generate some electrons, which are transmitted through a small hole in the bottom and then in a scintillator Eljen thechnilogy (EJ-204) flashes some photons in the process. These ligth is detected in a Hammamatzu r-647 photomultiplier (PM). The voltage output of the PM is controlled by a fast analogue-to-digital converter, and it is used at $900V$ voltage. The cup and the drift-scintellator tube was set at high voltages, $-17000V$ and -4000 respectively.

2.5 Lt detector

The Langmuir-Taylor detector (LT detector) chamber consists of a small CF40-6-way chamber. The detector consists essentially of an annealing filament, which is located between two planar round electrodes. The Operating Principle of an LT-Detector is based on surface ionization by the tunnel effect [12]. For the annealing filament is typically used rhenium, platinum or tungsten, as this is the most common due its comparatively high electron work function. With high voltages, the wire reaches high temperatures, as a consequence, a passing neutral atom is ionized, releasing an electron into the wire. The resulting ions are attracted by the negative electrodes

around the wire generating a current. The ionic current generated at the electrodes is proportional to the number of ionized atoms and is measured using a pico ammeter. The LT chamber is connected to the VMI chamber via an orifice plate and is used mainly as a beamdump and to align the detector. The most current generated in the chamber the most atoms are passing through the hole, so we can be sure that the beam pad is in the detection area.

3 Acquisition and calibration methods.

In order to use the above setup with the MIR and NIR laser parameters, the methods used in this experiment are explained in this section, from the VMI calibrartion thecniques to the data analisis ands post software analiosis process. All experimental techniques were used to investigate both helium and neon clusters.

In contrast to other spectroscopic experiments, the Photoelectric spectra (PES) of the $e-$ VMI, looks different for each event. We assume it happend because of the size distribution of the clusters and the different intensities each cluster is exposed to, comparing the small size of the cluster compared to the laser focus. Nevertheless, the images and therefore the PES look rather similar in shape for the small clusters. For larger clusters ($< N >= 10^6$) different shapes show up, as show in the results section. For example some images show blops compleates uniform while others signal, shoe ghiegh intensities in the edges and lower in the centewr, like a "donut" shape as we will refeer from now.

When recording single events with both, the TOF and the VMI spectrometer, it would be desirable if both spectra could be matched and lead back to the same event. A method is described in the following section. The disadvantage of this method is, that the maximum acquisition rate is maximum 30Hz, which is the speed of the camera. Depending on the hard drive, that is used the acquisition rate can drop to 10Hz. Furthermore, the single shot method needs low even trates of less then 10%. In total it results in an event rate of less then 1Hz.

3.1 Camera and trigger protocol

One of the main goal of this research, is to achieve individual data for single shots nanoplasma explosion in the VMI and TOF. The advantage, is the ability of the threat the data in a separate way to reduce the background and achieve properties on the coulomb explosion that are not possible when data is averaged.

Two methods were developed for this work. A first approach was done using a

Figure 3.1: Example images of MIr Vmi signal. On the left, a uniform blop, on the rigth a "donut " shape signal with high density signal on the borders of the edges.
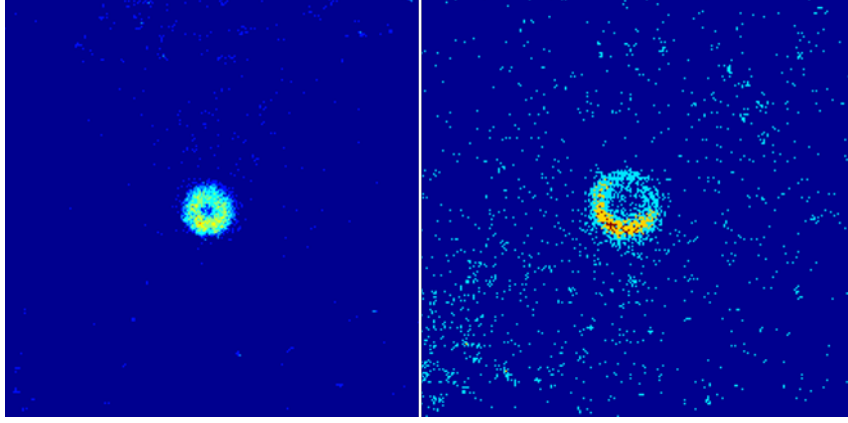
<div align="center">List delays</div>

Channel	Set to:
A	$= T + 0$
B	$= T + 1\mu s$
C	$= B or B + 6\mu s$

software trigger for the CCD camera and the oscilloscope for the TOF, an Acqiris Card CC103. Using LabView, an external clock (a RasberryPi 3) was triggered by the laser, the beginning of the explosion, at the same time, it software-trigger the camera and oscilloscope programs to start the acquisition. Having all the data acquired in the same software would allow to sort the data online and reduce the storage needed for the experiment. The Labview program was tested unsuccessfully for the data acquisition rate needed in ELI $100KHz$, the main problem was, that when a software-triggering scheme is used, extra delays are applied due to the operating system and the communication protocols, so even the data were acquired at the same time the delays in at saving it in the hard drive made impossible to correlate the signals.

Based on that same idea, a second approach was used. As alternative of the software triggering a hardware triggering was used. The laser triggers a delay generator that at the same time triggers the oscilloscope, a $R.S$ RTO2000 with bandwidth of 600MHZ to 6GHz, and the camera. Two facts had to be taken into account, first, the minimal exposure time of the camera is $34\mu s$. Second, the timing between the camera receiving the trigger and the real start of the acquisition is not negligible as it is for the oscilloscope. The camera took between $5-6\mu s$ to start after the trigger was sent. To solve this problem the triggering scheme in fig **??**.

A delay generator (Stanford Research Systems MD DG335) receives the laser

trigger (100KHz) channel B and C were connected to the oscilloscope to channel 1 and 2 respectively, and channel A was connected to the pin 1 (trigger) on the camera. Due the limitation of exposure time of the camera, we can not identify a single laser shot with it. Table **??** shows the delays used in the experiment, where T is the original laser trigger and A, B and C are the channels in the delay generator. In this way, it can be shown in fig, that the oscilloscope can "see" each of the laser shots individually but the camera will see at least 3 shots, but fortunately, not each laser shot generates signal, as show in the next chapter in general just $10 to 20\%$ of the laser short ignites a plasma explosion, this mean that most of the pictures will have no signal, rare cases will have two or more explosion and the pictures with actual signal will contain just one explosion in the VMI that can be correlated to its individual TOF signal.
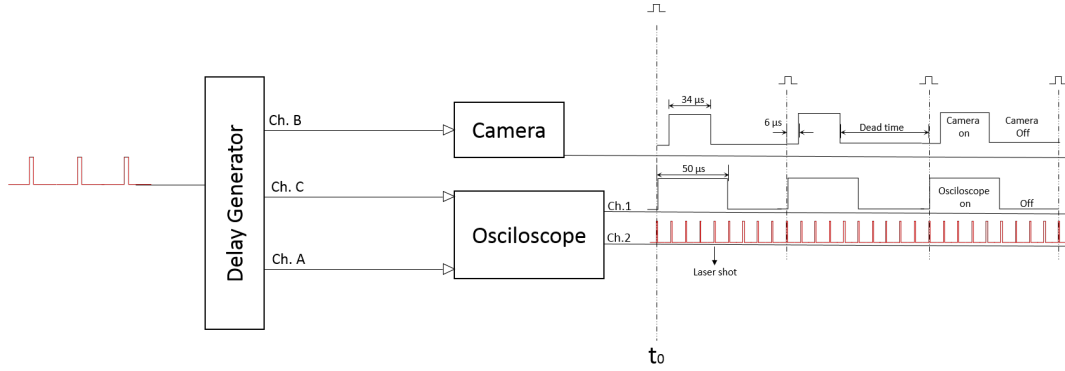
Figure 3.2: Scheme of the trigger system used.

In Fig **??**, we show the Trigger scheme used in the experiment. The oscilloscope and camera are triggered by the delayed channel B. The oscilloscope is set to $50\mu s$ and the camera to the minimal exposure time. So the camera and oscilloscope sees the same trigger, the oscilloscope will record at least 5 laser shots, but the camera because starts later just can see three as shown. The pictures are saved in the memory RAM of the computer so the dead time after the camera is off is mandatory to give the operating system enough time to save the data on disk and don't get out of ram. A small improvement in this system can be done if we trigger the camera with B and the oscilloscope with C, so both apparatus can start almost at the same time and no corrections need to be done. Each of the data set are saved with a unique label that will help to correlate the data after. Once an explosion is found in the VMI pictures, we check in its corresponding TOF that it has just one signal in all five laser shots, so we can be sure that picture correspond to a single coulomb explosion, in case more than one signal is found, this picture is discarded.

3.2 Calibration methods

3.2.1 VMI calibration

To calibrate the VMI spectrometer,two different methods were used. A quadratic calibration function $E = \alpha \cdot r^2$ is used, where E is the kinetic energy of the particles and r is the measured radius. This function is chosen because $E_{kin} = 1/2 \cdot mv^2$. In order to keep simplicity, stray fields, third order or linear terms are not included, as long as the calibration curves fit well with the measured.

On one hand, the most independant method is the trajectory simulation, because it does not rely on any lasersystem or physical process. Those simulations were made with SIMION 8.1. For the starting conditions for the electrons we chose a small interaction volume comparable to the estimated experimental conditions and the emission direction perpedicular to the spectrometer axis. For those electrons the projected energy on the detector screen is equivalent to the real kinetic energy, with this the inverse abel transformation can be avoided. It is neccessay to simulate different kinetic energies for the electrons, at different velocity vectors. After extracting the radii, where the electrons hit the detector plane, a calibration from pixels to mm for the camera is needed, because SIMION gives the radii of the electrons in mm. To do so, known distance in the camera image is needed, for example the inner diameter of the phosphor screen, making possible to generate the fit curve. The disadvantage of this method is, that it is very difficult to include any magnetic or electric stray fields into the simultions or other external parameter that can be in real.
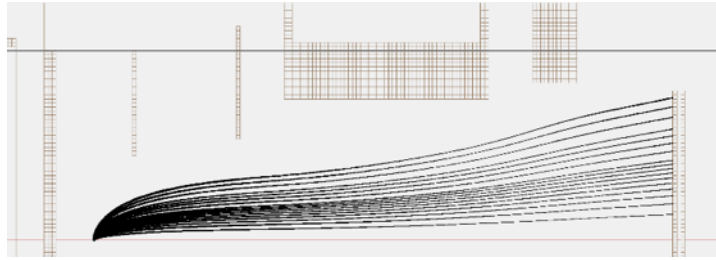
Figure 3.3: energy calibration of the VMI spectrometer with SIMION. Electrons with discrete kinetic energy are emitted perpendicular to the spectrometer axis.

On the other hand, in order to contrast the simulation, a physical process is used, creating electrons with a well-known energy, then above threshold ionization (ATI) of raregas atoms is a suitable method to calibrate the spectrometer. The details about ATI of xenon can be found here xxx. The result of the ATI mechanism are several rings in the VMI along the laser polarization axis, that are energetically

spaced by the energy of one photon. With at least 2 rings visible it is possible to do the calibration with the following formula

$$\Delta E = \alpha(r_2^2 - r_1^2)$$

where ΔE is the poton energy, r_i are the peak positions of the abel inverted rings and α the calibration factor. Best results are achieved by using as low peak intensities as possible, so tunnel ionization is suppressed.
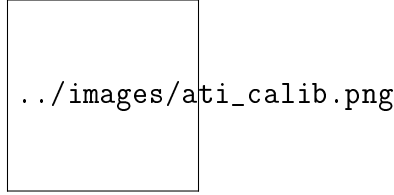

Figure 3.4: energy calibration of the VMI spectrometer with the ATI method. The fringes are seperated by one photon energy, in this case 1.55eV

Another method to calibrate a VMI spectrometer is the use of a narrowband laser in combination with resonant processes. A very usefull scheme is published by *Wituschek et al.* [?]. The scheme uses continuous 404nm laserlight to excite either the $5p_{3/2}$ or the $5p_{1/2}$ state in potassium. From this state, relaxation in four other states and the groundstate is possible. The 404nm light can also ionize electons from the resonant 5p state, the 5s, the 3d and the 4p states. The resulting electrons carry a very well defined kinetic energy $E_{kin} = E_{Photon} + E_{state} - E_{ionization}$. Since all energies on the right side of the equation are well known, the kinetic energy is also well known. This allows the calibration of the spectrometer with three points (the cross section of the 5s state is too small to see it) in the low energy range.

3.2.2 Laser intensity calibration

When using a focused MIR and NIR laser, it is essential to know the peak intensity in the focus of the laserfield. Most of the time calculations give wrong results, because they assume a perfectly gaussian shape and do not account losses in optics after the power measurement or an inperfect focus. So it would be desirable to avoid caluclations and measure the peak intensity direclty. In this thesis two different schemes are used, the $2U_P$ cutoff energy of electrons in a laserfield [?], [2] and the ratios of charge states of ions produced in the laser field [?].
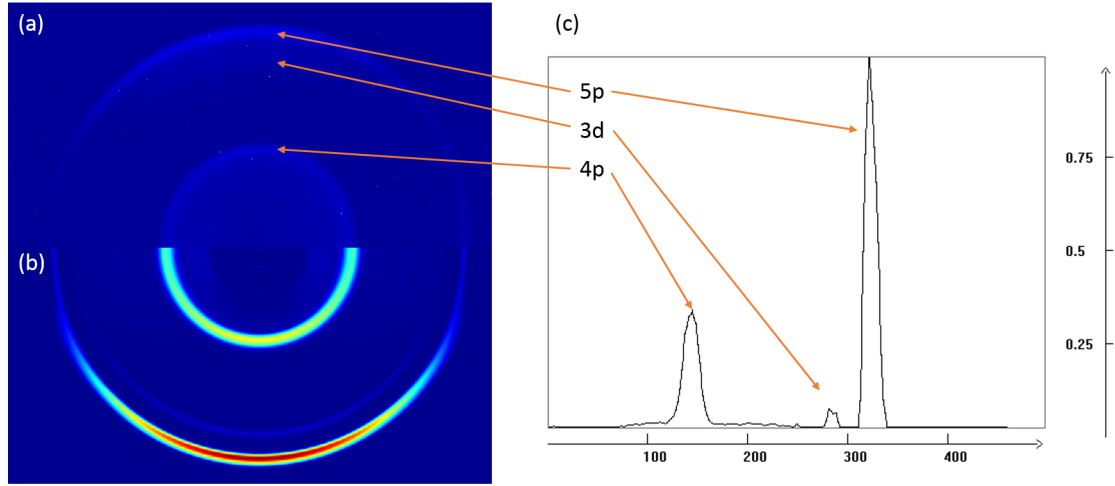
Figure 3.5: (a) Photoelectron image of potassium excited and ionized by linear polarized 404nm light, (b) abel inverted image and (c) corresponding photoelectron spectrum, not yet calibrated on the energy

3.3 Coulomb Explosion Model

To explain the central feature in figure XXX a model for a coulomb explosion model from XXX is apllied. In this model a homogeniously charged sphere with radius R is asumed and the charge distribution is given as a probability density function

$$\frac{dP}{dr} = \frac{3r^2}{R^3}\Theta(R-r) \tag{3.1}$$

where, $\frac{dP}{dr}$ is the probability to find an electron at radius r and Θ is the Heavyside function. For this system the coulomb energy distribution E_{coul} reads

$$E_{coul}(r) = Ne^2\frac{r^2}{R^3} \tag{3.2}$$

for $r \leq R$. N is the number of electrons in the sphere and e is the elementary charge of an electron. A charged sphere like this will immediately coulomb explode and for $t \longrightarrow \infty$ all coulomb energy is converted to kinetic energy, which can be measured experimentally with the VMI. It is possible to retrieve the energy distribution out of the spacial distribution 3.1 with 3.2 as the substitution formula.

$$dr = \frac{R^3}{2Nq^2r}dE \tag{3.3}$$

Furthermore, we define the maximum coulomb energy

$$E(R) := E_R = Nq^2 \frac{1}{R} \tag{3.4}$$

with all this follows the energy distribution of the electrons

$$\frac{dP}{dE} = \frac{3}{2}\sqrt{\frac{1}{E_R}}\frac{1}{E_R}\sqrt{E} \cdot \Theta(1 - \frac{E}{E_R}) \tag{3.5}$$

it can be seen, that the energy distribution is fully characterized by E_R, so it is enough to know the maxium kinetic energy, which is just the radius of the central feature in our VMI images. With this even the inverse abel transformation can be bypassed, because the edge of a sphere in invariant for projecting the sphere on a plane.

With the formula for the homogenius density in a sphere

$$R = (\frac{N}{\frac{4}{3}\pi\rho})^{1/3} \tag{3.6}$$

and formula 3.4 the charge density in the beginning in the process can be derived to

$$E_{max}(N) = \underbrace{\frac{e^2}{4\pi\epsilon_0}(\frac{4}{3}\pi\rho)^{1/3}}_{=:B} N^{2/3} \tag{3.7}$$

and with this the charge density reads

$$\rho = 48\pi^2 \frac{\epsilon_0^3}{e^6} B^3 \tag{3.8}$$

In summary, the charge density can be calculated with the fit parameter B. B can be retrieved by plotting the maximum kinetic energy E_R as a function of the number of electrons N. Both can be extracted out of the VMI images, E_R from the radius and N from the brightness of the central feature.

3.4 data analisis

The High laser repetition rate compared to the Lor explsosion rate mentioned above, leads to a huge amoung of empty data. in oder wors , less than 10% of all vmi pictures and TOF spectra didn conain any nanoplasma explosion. So a signal finder procesing, in mathematica software, was impplemented. In the next section we will explain the signal recognition algorithms and the data processing, as well as the first assumption of our model to explaing the threatment given to the results.

3.4.1 Event recognision

As mentioned, the low event rate of nano plasma explosions results in a lot of emtpy VMI images. In average 10000 pictures where taken for each set of data where, less than 7% of them contain signal, in the best systems. A typical VMI signal can be seen in fig 3.1, where regarding if its NIR or MIR, a central feature with circular distribution is presented. However, the angular an radial distribution changes, depending of the experiment. When the uncoupled mode of the spectrometers is used, like in the NIR measurements, the VMI images have to be sorted without the help of the TOF traces.

To seperate empty images from images with events the central feature is used. A center is selected manually and all pixels within a region around the center are summed up. If the sum is above a certain threshold value the image contains a signal. To analyze the central feature in more detail the size and the brightness of this feature is of importance. To determine the radius and the brightness, two methods were compared, one using the mathematica 10.1 (wolfram inc.) algorithm and the other using a bining processing., both explained on next.

First, the ImageMeasurements and Componentmeasurements algoriths in mathematica act, over binnirized images, works with arbitrary 2D and 3D images and computes multiple porperties, finding components bases on an specifc matrix. For this special case, a circular matrix with specifications of minimun radius and no share edges were given as paramneters. The efficient of this process was demostrared to depent stronglly on the initial image and the signal-noise rate, hence, a recursive funtion when develop to change the binarized threshold recursively until the algprithm find just one object that matchs the signal. The thrshold was changed progresively and modifyable steps in order to get the most precise fit. Once the object is found, the radius and center are save, and sum the total intensity inside the radius, so a radius-Brigthness meassument ius compleat for each invividual image.

The secon method was based on a circula binning of the signal. A center for each
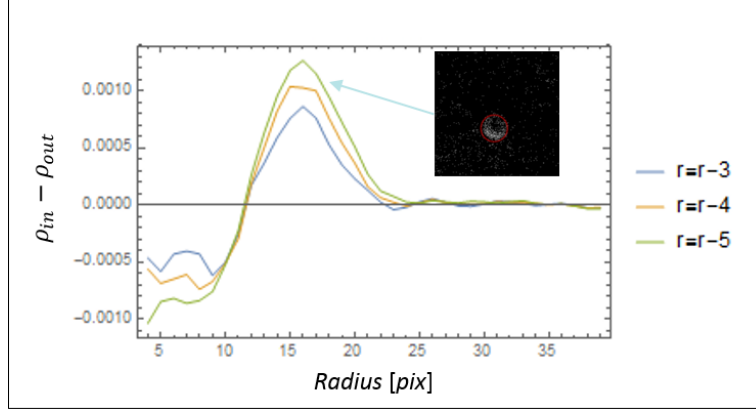
Figure 3.6: Difference of mean pixel values to determine the radius of the central feature in the VMI images

data set is manually place afte summed all signal pictures and find the center of the signal blop, set to be at the same position within one measurement. Three circles are defined around this center, the first one with radius r (in pixels), which is variale, the second one with $r_{in} = r - \Delta r$ and the last one with $r_{out} = r + \Delta r$, where Δr has to be picked out from the dataset. The three circles define two areas A_{in} and A_{out}, see figure XXX. An average pixelvalue ρ for both areas is defined via

$$\rho_{in} = \frac{1}{N_{in}} \sum_{px \in A_{in}} \text{value}(px) \tag{3.9}$$

$$\rho_{out} = \frac{1}{N_{out}} \sum_{px \in A_{out}} \text{value}(px) \tag{3.10}$$

where N is the number of pixels in the respective area. The normalization on the area is important, because the areas are of different size. To finally find out the radius of the central blop, the difference $\rho_{in} - \rho_{in}$ is maximized, this is the case for the orange box in figure XXX. For the green and the purple boxes $\rho_{in} = \rho_{in}$, which gives zero for the difference. Real signals do not have a perfect cutoff or a constant radial profile, which leads to noisy curves, when Δr is chosen too small, which makes the determination of r difficult. An example for a single shot image, where the radius is determined for $\Delta r = 3, 4, 5$ in pixels, is shown in figure 3.6. The VMI image in this figure has a donut shape, if the inner radius is of interest the same curve can be used to determine the inner radius as well if the minimum of the function is taken.

As shown in 3.6, the density difference have a sumit in tho cases, one when the inner our outer density changes signs. The lower peak, when exists, reffers to the

change from a low density change to a high one, besides the higher peak, describe the change from a high desnsity to a lower, setting the radius where the edge of the blop is. pointing out that not all signals have the donut shape so this case was just added when needed. Finally, as in the last procedure, the inner pixels in the circle with radius r are summed and the radius-Brigthnes is save for all signal. In the case, as the example, where the second inner circle is clearly identified, the sum of all the pixel discard the inner are, and at the same time, adds the inner radius-brightness measurements to it. Both radius finder functions where always double checked by taking random signal images and highlighting the radius found. Figure 3.7 shows a set of well fitted radius for each signal, proving the good efficiency of the algorithms.

Figure 3.7: Example of ramdom signal images fitted to ir corresponding radius.
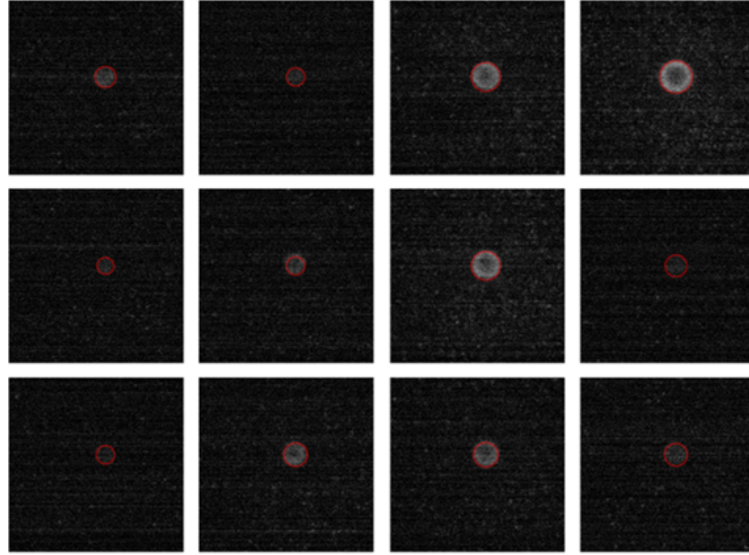
Last, once the radius-brightness data is recorded, and the calibrations are set, the system can be compare to the model explained above, where radius can be converted itio maximal kinetic energy, $r \to k_{energy}$, and brightness to number of electrons, $b \to N_{e-}$.

List of Figures

List of Tables

4 Bibliography

[1] *Helium.* http://ltl.tkk.fi/research/theory/helium.html

[2] BECKER, U. (Hrsg.) ; SHIRLEY, D. A. (Hrsg.): *VUV and Soft X-Ray Photoionization.* http://dx.doi.org/10.1007/978-1-4613-0315-2

[3] A. BETHE, H. ; E. SALPETER, E. : *The Quantum Mechanics of One- and Two-Electron Atoms.* Bd. 35. http://dx.doi.org/10.1007/978-3-662-12869-5. http://dx.doi.org/10.1007/978-3-662-12869-5

[4] ATKINS, K. R.: *Liquid Helium.* Cambridge University Press. – ISBN 978–1–107–63890–7. – Google-Books-ID: gzmNAwAAQBAJ

[5] BERKOWITZ, J. : *Photoabsorption, photoionization, and photoelectron spectroscopy.* Academic Press. – ISBN 978–0–12–091650–4. – Google-Books-ID: POeHAAAAIAAJ

[6] BÜNERMANN, O. ; STIENKEMEIER, F. : Modeling the formation of alkali clusters attached to helium nanodroplets and the abundance of high-spin states. 61, Nr. 3, 645–655. http://dx.doi.org/10.1140/epjd/e2011-10466-0. – DOI 10.1140/epjd/e2011–10466–0. – ISSN 1434–6079

[7] BUCHENAU, H. ; KNUTH, E. L. ; NORTHBY, J. ; TOENNIES, J. P. ; WINKLER, C. : Mass spectra and time-of-flight distributions of helium cluster beams. 92, Nr. 11, 6875–6889. http://dx.doi.org/10.1063/1.458275. – DOI 10.1063/1.458275. – ISSN 0021–9606, 1089–7690

[8] CHRISTEN, W. ; RADEMANN, K. ; EVEN, U. : Supersonic Beams at High Particle Densities: Model Description beyond the Ideal Gas Approximation [†]. 114, Nr. 42, 11189–11201. http://dx.doi.org/10.1021/jp102855m. – DOI 10.1021/jp102855m. – ISSN 1089–5639, 1520–5215

[9] CONNERADE, J. P.: *Highly Excited Atoms.* Cambridge University Press. – ISBN 978–0–521–43232–0. – Google-Books-ID: VgpkXDfkqYEC

[10] DALY, N. R.: Scintillation Type Mass Spectrometer Ion Detector. 31, Nr. 3, 264–267. http://dx.doi.org/10.1063/1.1716953. – DOI 10.1063/1.1716953. – ISSN 0034–6748

[11] DELFT, D. van ; KES, P. : The discovery of superconductivity. 63, Nr. 9, 38–43. http://dx.doi.org/10.1063/1.3490499. – DOI 10.1063/1.3490499. – ISSN 0031–9228

[12] DELHUILLE, R. ; MIFFRE, A. ; LAVALLETTE, E. ; BÜCHNER, M. ; RIZZO, C. ; TRÉNEC, G. ; VIGUÉ, J. ; LOESCH, H. J. ; GAUYACQ, J. P.: Optimization of a Langmuir–Taylor detector for lithium. 73, Nr. 6, 2249–2258. http://dx.doi.org/10.1063/1.1472467. – DOI 10.1063/1.1472467. – ISSN 0034–6748

[13] DITMIRE, T. ; DONNELLY, T. ; RUBENCHIK, A. M. ; FALCONE, R. W. ; PERRY, M. D.: Interaction of intense laser pulses with atomic clusters. 53, Nr. 5, 3379–3402. http://dx.doi.org/10.1103/PhysRevA.53.3379. – DOI 10.1103/PhysRevA.53.3379

[14] EINSTEIN, A. : Über einen die Erzeugung und Verwandlung des Lichtes betreffenden heuristischen Gesichtspunkt. 322, Nr. 6, 132–148. http://dx.doi.org/10.1002/andp.19053220607. – DOI 10.1002/andp.19053220607. – ISSN 1521–3889

[15] ENSS, C. ; HUNKLINGER, S. : Low-Temperature Physics. Springer-Verlag //www.springer.com/de/book/9783540231646. – ISBN 978–3–540–23164–6

[16] EPPINK, A. T. J. B. ; PARKER, D. H.: Velocity map imaging of ions and electrons using electrostatic lenses: Application in photoelectron and photofragment ion imaging of molecular oxygen. 68, Nr. 9, 3477–3484. http://dx.doi.org/10.1063/1.1148310. – DOI 10.1063/1.1148310. – ISSN 0034–6748

[17] ERK, B. : Nobel cluster gas expansion driven by a ultra-short high intensity infrared laser

[18] FENNEL, T. ; MEIWES-BROER, K.-H. ; TIGGESBÄUMKER, J. ; REINHARD, P.-G. ; DINH, P. M. ; SURAUD, E. : Laser-driven nonlinear cluster dynamics. 82, Nr. 2, 1793–1842. http://dx.doi.org/10.1103/RevModPhys.82.1793. – DOI 10.1103/RevModPhys.82.1793

[19] FERMI, E. : Quantum Theory of Radiation. 4, Nr. 1, 87–132. http://dx.doi.org/10.1103/RevModPhys.4.87. – DOI 10.1103/RevModPhys.4.87

[20] GAVEAU, M.-A. ; BRIANT, M. ; VALLET, V. ; M. MESTDAGH, J. ; P. VISTICOT, J. : Reaction Between Barium and N2O on Large Neon Clusters. http://dx.doi.org/10.1007/978-3-642-56800-8_57. – DOI 10.1007/978–3–642–56800–8$_5$7. $- - ISBN 978 - -3 - -642 - -63150 - -4, S.827 - -838$

[21] GOUGH, T. E. ; MENGEL, M. ; ROWNTREE, P. A. ; SCOLES, G. : Infrared spectroscopy at the surface of clusters: SF6 on Ar. 83, Nr. 10, 4958–4961. http://dx.doi.org/10.1063/1.449757. – DOI 10.1063/1.449757. – ISSN 0021–9606

[22] GREBENEV, S. ; TOENNIES, J. P. ; VILESOV, A. F.: Superfluidity Within a Small Helium-4 Cluster: The Microscopic Andronikashvili Experiment. 279, Nr. 5359, 2083–2086. http://dx.doi.org/10.1126/science.279.5359.2083. – DOI 10.1126/science.279.5359.2083. – ISSN 0036–8075, 1095–9203

[23] GRIFFITHS, D. J.: *Introduction to electrodynamics*. Fourth edition. Pearson. – ISBN 978–0–321–85656–2

[24] GRÜNER, B. : *Femtosekundenspektroskopie an dotierten Heliumnanotröpfchen: Dissipative Vibrationsdynamik und Charakterisierung eines Nanoplasmas*

[25] HAGENA, O. F. ; OBERT, W. : Cluster Formation in Expanding Supersonic Jets: Effect of Pressure, Temperature, Nozzle Size, and Test Gas. 56, Nr. 5, 1793–1802. http://dx.doi.org/10.1063/1.1677455. – DOI 10.1063/1.1677455. – ISSN 0021–9606

[26] HAGENA, O. F. ; OBERT, W. : Cluster Formation in Expanding Supersonic Jets: Effect of Pressure, Temperature, Nozzle Size, and Test Gas. 56, Nr. 5, 1793–1802. http://dx.doi.org/10.1063/1.1677455. – DOI 10.1063/1.1677455. – ISSN 0021–9606

[27] HALPERIN, W. P. ; RASMUSSEN, F. B. ; ARCHIE, C. N. ; RICHARDSON, R. C.: Properties of melting 3He: Specific heat, entropy, latent heat, and temperature. 31, Nr. 5, 617–698. http://dx.doi.org/10.1007/BF00116046. – DOI 10.1007/BF00116046. – ISSN 1573–7357

[28] HARMS, J. ; TOENNIES, J. P. ; DALFOVO, F. : Density of superfluid helium droplets. 58, Nr. 6, 3341–3350. http://dx.doi.org/10.1103/PhysRevB.58.3341. – DOI 10.1103/PhysRevB.58.3341

[29] HAUGHT, A. F. ; POLK, D. H.: Formation and Heating of Laser Irradiated Solid Particle Plasmas. 13, Nr. 11, 2825–2841. http://dx.doi.org/10.1063/1.1692869. – DOI 10.1063/1.1692869. – ISSN 0031–9171

[30] HEIDENREICH, A. ; GRÜNER, B. ; SCHOMAS, D. ; STIENKEMEIER, F. ; KRISHNAN, S. R. ; MUDRICH, M. : Charging dynamics of dopants in helium nanoplasmas. http://dx.doi.org/10.1080/09500340.2017.1281454. – DOI 10.1080/09500340.2017.1281454

[31] KAMENEV, A. : Introduction to the Keldysh Formalism.

[32] KAPITZA, P. : Viscosity of Liquid Helium below the -Point. 141, Nr. 3558, 74. http://dx.doi.org/10.1038/141074a0. – DOI 10.1038/141074a0. – ISSN 1476–4687

[33] KARNAKOV, B. M. ; MUR, V. D. ; POPRUZHENKO, S. V. ; POPOV, V. S.: Strong field ionization by ultrashort laser pulses: Application of the Keldysh theory. 374, Nr. 2, 386–390. http://dx.doi.org/10.1016/j.physleta.2009.10.058. – DOI 10.1016/j.physleta.2009.10.058. – ISSN 0375–9601

[34] KELDYSH, L. V.: Ionization in the field of a strong electromagnetic wave. 20, 1307. https://ci.nii.ac.jp/naid/10006486551/

[35] KNUTH, E. L. ; HENNE, U. : Average size and size distribution of large droplets produced in a free-jet expansion of a liquid. 110, Nr. 5, 2664–2668. http://dx.doi.org/10.1063/1.477988. – DOI 10.1063/1.477988. – ISSN 0021–9606, 1089–7690

[36] KRISHNAN, S. R. ; FECHNER, L. ; KREMER, M. ; SHARMA, V. ; FISCHER, B. ; CAMUS, N. ; JHA, J. ; KRISHNAMURTHY, M. ; PFEIFER, T. ; MOSHAMMER, R. ; ULLRICH, J. ; STIENKEMEIER, F. ; MUDRICH, M. : Ignition of Doped Helium Nanodroplets in Intense Few-Cycle Laser Pulses. In: YAMANOUCHI, K. (Hrsg.) ; KATSUMI, M. (Hrsg.): *Multiphoton Processes and Attosecond Physics*, Springer Berlin Heidelberg (Springer Proceedings in Physics). – ISBN 978–3–642–28948–4, S. 385–390

[37] KRISHNAN, S. R.: Doped helium nanodroplets in intense few-cycle infrared pulses. http://inis.iaea.org/Search/search.aspx?orig_q=RN:43095633

[38] LAST, I. ; JORTNER, J. : Quasiresonance ionization of large multicharged clusters in a strong laser field. 60, Nr. 3, 2215–2221. http://dx.doi.org/10.1103/PhysRevA.60.2215. – DOI 10.1103/PhysRevA.60.2215

[39] LEWERENZ, M. ; SCHILLING, B. ; TOENNIES, J. P.: Successive capture and coagulation of atoms and molecules to small clusters in large liquid helium clusters. 102, Nr. 20, 8191–8207. http://dx.doi.org/10.1063/1.469231. – DOI 10.1063/1.469231. – ISSN 0021–9606

[40] LEWIS, W. K. ; HARRUFF-MILLER, B. A. ; LEATHERMAN, P. ; GORD, M. A. ; BUNKER, C. E.: Helium droplet calorimetry of strongly bound species: Carbon clusters from C_2 to C_{12}. 85, Nr. 9, 094102. http://dx.doi.org/10.1063/1.4895670. – DOI 10.1063/1.4895670. – ISSN 0034–6748, 1089–7623

[41] MADISON, K. W. ; PATEL, P. K. ; ALLEN, M. ; PRICE, D. ; FITZPATRICK, R. ; DITMIRE, T. : Role of laser-pulse duration in the neutron yield of deuterium cluster targets. 70, Nr. 5. http://dx.doi.org/10.1103/PhysRevA.70.053201. – DOI 10.1103/PhysRevA.70.053201. – ISSN 1050–2947, 1094–1622

[42] MAINFRAY, G. : MULTIPHOTON IONIZATION OF ATOMS.

[43] MÖBIUS, E. ; GALVIN, A. B. ; KISTLER, L. M. ; KUCHAREK, H. ; POPECKI, M. A.: Time-of-flight mass spectrographs—From ions to neutral atoms. 121, Nr. 12, 11,647–11,666. http://dx.doi.org/10.1002/2016JA022553. – DOI 10.1002/2016JA022553. – ISSN 2169–9402

[44] MEIJA, J. ; COPLEN, T. B. ; BERGLUND, M. ; BRAND, W. A. ; DE, B. P. ; GRÖNING, M. ; HOLDEN, N. E. ; IRRGEHER, J. ; LOSS, R. D. ; WALCZYK, T. ; PROHASKA, T. : Atomic weights of the elements 2013 (IUPAC Technical Report). 88, Nr. 3, 265–291. http://dx.doi.org/10.1515/pac-2015-0305. – DOI 10.1515/pac–2015–0305. – ISSN 0033–4545

[45] MIKABERIDZE, A. : *Atomic and molecular clusters in intense laser pulses.* https://www.pks.mpg.de/mpi-doc/rostgruppe/dissertation/mikaberidze_dissertation.pdf

[46] NAUTA, K. ; MILLER, R. E.: Nonequilibrium Self-Assembly of Long Chains of Polar Molecules in Superfluid Helium. 283, Nr. 5409, 1895–1897. http://dx.doi.org/10.1126/science.283.5409.1895. – DOI 10.1126/science.283.5409.1895. – ISSN 0036–8075, 1095–9203

[47] PIETROWSKI, R. von ; RUTZEN, M. ; HAEFTEN, K. von ; KAKAR, S. ; MÖLLER, T. : Fluorescence excitation spectroscopy of Xenon doped Neon clusters: Size and site effects, and cluster melting. 40, S. 22–24. http://dx.doi.org/10.1007/s004600050149. – DOI 10.1007/s004600050149

[48] POPRUZHENKO, S. V.: Keldysh theory of strong field ionization: history, applications, difficulties and perspectives. 47, Nr. 20, 204001. `http://dx.doi.org/10.1088/0953-4075/47/20/204001`. – DOI 10.1088/0953–4075/47/20/204001. – ISSN 0953–4075

[49] PROTOPAPAS, M. ; KEITEL, C. H. ; KNIGHT, P. L.: Atomic physics with super-high intensity lasers. 60, Nr. 4, 389–486. `http://dx.doi.org/10.1088/0034-4885/60/4/001`. – DOI 10.1088/0034–4885/60/4/001. – ISSN 0034–4885, 1361–6633

[50] RAFIPOOR, A. J. M.: *Two-Color Photoionization Experiments with Ultrashort Light Pulses on Small Atomic Systems*

[51] RHODES, C. K.: Multiphoton Ionization of Atoms. 229, Nr. 4720, 1345–1351. `http://dx.doi.org/10.1126/science.229.4720.1345`. – DOI 10.1126/science.229.4720.1345. – ISSN 0036–8075, 1095–9203

[52] SAALMANN, U. ; SIEDSCHLAG, C. ; ROST, J. M.: Mechanisms of cluster ionization in strong laser pulses. 39, Nr. 4, R39–R77. `http://dx.doi.org/10.1088/0953-4075/39/4/R01`. – DOI 10.1088/0953–4075/39/4/R01. – ISSN 0953–4075, 1361–6455

[53] SCHMIDT, V. : *Electron Spectrometry of Atoms using Synchrotron Radiation*. Cambridge University Press. – ISBN 978–0–521–55053–6

[54] SCHOMAS, D. ; RENDLER, N. ; KRULL, J. ; RICHTER, R. ; MUDRICH, M. : A compact design for velocity-map imaging of energetic electrons and ions. 147, Nr. 1. `http://dx.doi.org/10.1063/1.4984076`. – DOI 10.1063/1.4984076. – ISSN 0021–9606

[55] STEBBINGS, S. L. ; SÜSSMANN, F. ; YANG, Y.-Y. ; SCRINZI, A. ; DURACH, M. ; RUSINA, A. ; STOCKMAN, M. I. ; KLING, M. F.: Generation of isolated attosecond extreme ultraviolet pulses employing nanoplasmonic field enhancement: optimization of coupled ellipsoids. 13, Nr. 7, 073010. `http://dx.doi.org/10.1088/1367-2630/13/7/073010`. – DOI 10.1088/1367–2630/13/7/073010. – ISSN 1367–2630

[56] STIENKEMEIER, F. ; LEHMANN, K. K.: Spectroscopy and dynamics in helium nanodroplets. 39, Nr. 8, R127–R166. `http://dx.doi.org/10.1088/0953-4075/39/8/R01`. – DOI 10.1088/0953–4075/39/8/R01. – ISSN 0953–4075, 1361–6455

[57] STRINGARI, S. ; TREINER, J. : Systematics of liquid helium clusters. 87, Nr. 8, 5021–5027. http://dx.doi.org/10.1063/1.452818. – DOI 10.1063/1.452818. – ISSN 0021–9606

[58] SWENSON, C. A.: The Liquid-Solid Transformation in Helium near Absolute Zero. 79, Nr. 4, 626–631. http://dx.doi.org/10.1103/PhysRev.79.626. – DOI 10.1103/PhysRev.79.626

[59] TCHAPLYGUINE, M. ; LUNDWALL, M. ; GISSELBRECHT, M. ; ÖHRWALL, G. ; FEIFEL, R. ; SORENSEN, S. ; SVENSSON, S. ; MÅRTENSSON, N. ; BJÖRNEHOLM, O. : Variable surface composition and radial interface formation in self-assembled free, mixed ArXe clusters. 69, Nr. 3, 031201. http://dx.doi.org/10.1103/PhysRevA.69.031201. – DOI 10.1103/PhysRevA.69.031201

[60] TOENNIES, J. P. ; VILESOV, A. F.: Spectroscopy of Atoms and Molecules in Liquid Helium. 49, Nr. 1, 1–41. http://dx.doi.org/10.1146/annurev.physchem.49.1.1. – DOI 10.1146/annurev.physchem.49.1.1

[61] TOENNIES, J. P. ; VILESOV, A. F.: Superfluid Helium Droplets: A Uniquely Cold Nanomatrix for Molecules and Molecular Complexes. 43, Nr. 20, 2622–2648. http://dx.doi.org/10.1002/anie.200300611. – DOI 10.1002/anie.200300611. – ISSN 1521–3773

[62] WABNITZ, H. ; BITTNER, L. ; CASTRO, A. R. B. ; DÖHRMANN, R. ; GÜRTLER, P. ; LAARMANN, T. ; LAASCH, W. ; SCHULZ, J. ; SWIDERSKI, A. ; HAEFTEN, K. von ; MÖLLER, T. ; FAATZ, B. ; FATEEV, A. ; FELDHAUS, J. ; GERTH, C. ; HAHN, U. ; SALDIN, E. ; SCHNEIDMILLER, E. ; SYTCHEV, K. ; TIEDTKE, K. ; TREUSCH, R. ; YURKOV, M. : Multiple ionization of atom clusters by intense soft X-rays from a free-electron laser. 420, Nr. 6915, 482–485. http://dx.doi.org/10.1038/nature01197. – DOI 10.1038/nature01197. – ISSN 1476–4687

[63] WEINBERGER, P. : The discovery of thermodynamics. 93, Nr. 20, 2576–2612. http://dx.doi.org/10.1080/14786435.2013.784402. – DOI 10.1080/14786435.2013.784402. – ISSN 1478–6435

[64] WHITTLE, E. ; DOWS, D. A. ; PIMENTEL, G. C.: Matrix Isolation Method for the Experimental Study of Unstable Species. 22, Nr. 11, 1943–1943. http://dx.doi.org/10.1063/1.1739957. – DOI 10.1063/1.1739957. – ISSN 0021–9606, 1089–7690

[65] WILEY, W. C. ; MCLAREN, I. H.: Time-of-Flight Mass Spectrometer with Improved Resolution. 26, Nr. 12, 1150–1157. http://dx.doi.org/10.1063/1.1715212. – DOI 10.1063/1.1715212. – ISSN 0034–6748

[66] YOUNG, D. A.: PHASE DIAGRAMS OF THE ELEMENTS.

[67] ZHAO, K. ; ZHANG, Q. ; CHINI, M. ; WU, Y. ; WANG, X. ; CHANG, Z. : Tailoring a 67 attosecond pulse through advantageous phase-mismatch. 37, Nr. 18, 3891–3893. http://dx.doi.org/10.1364/OL.37.003891. – DOI 10.1364/OL.37.003891. – ISSN 1539–4794

Danksagung

An dieser Stelle Danke

Erklärung

Ort, Datum ....   Unterschrift ....